ABSTRACT

Power-amplifier Optimization Using Tunable Circuitry and Stability Analysis Methods for the Next Generation Radar

Lucilia R. Hays, M.S.E.C.E.

Mentor: Charles P. Baylis II, Ph.D.

In response to the increasingly congested and contested wireless spectrum, the next generation radar must be adaptive and reconfigurable. A reconfigurable power-amplifier is a necessary component of the cognitive radar system. The reconfigurable power-amplifier must operate efficiently and stably while maintaining spectrum compliance. The research in this thesis presents state-of-the-art tuning algorithms for optimizing the load reflection coefficient presented to a transistor by novel tunable circuitry. The algorithms are implemented on a varactor diode network and a high-power handling evanescent mode cavity tuner as the tunable load matching networks. In addition, stability considerations are explored. A new amplifier design tool, the frequency Smith Tube, is presented which allows for broadband stability analysis for small-signal inputs. A real-time stability analysis procedure based on the acceleration of transducer gain during optimization is also presented.

Power Amplifier Optimization Using Tunable Circuitry and Stability Analysis Methods for the Next Generation Radar

by

Lucilia R. Hays, B.S.E.C.E.

A Thesis

Approved by the Department of Electrical and Computer Engineering

_____

Kwang Y. Lee, Ph.D., Chairperson

Submitted to the Graduate Faculty of
Baylor University in Partial Fulfillment of the
Requirements for the Degree
of

Master of Science in Electrical and Computer Engineering

Approved by the Thesis Committee

_____

Charles P. Baylis II, Ph.D., Chairperson

_____

Robert J. Marks II, Ph.D.

_____

Jill Klentzman, Ph.D.

Accepted by the Graduate School

May 2018

_____

J. Larry Lyon, Ph.D., Dean

Page bearing signatures is kept on file in the Graduate School.

TABLE OF CONTENTS

LIST OF FIGURES

LIST OF TABLES

ACKNOWLEDGMENTS

I would like to thank my research advisor, Dr. Charles Baylis, not only for the engineering expertise that he contributed to my work, but also for his support and encouragement of my intellectual and spiritual growth. I would also like to thank Dr. Robert Marks for his advice and guidance on this research. I would like to acknowledge and thank several collaborators from the Army Research Laboratory including John Clark, Edward Viveiros, John Penn, Khamsouk Kingkeo, Dr. Abigail Hedden, Dr. Ali Darwish, Dr. Anthony Martone, and Dr. Kyle Gallagher. Special thanks to John Clark for his help editing papers for publication and Edward Viveiros and Khamsouk Kingkeo for their help and mentorship during my summer internship at the Army Research Laboratory. I would like to thank our collaborators at Purdue University: Dr. Dimitrios Peroulis, Dr. Abbas Semnani, and Dr. Mohammad Abu-Khater. I would also especially like to thank my current collaborators at Baylor University – Zachary Hays, Casey Latham, Sarvin Rezayat, Pedro Rodriguez-Garcia, and Austin Egbert – as well as previous collaborators who have since graduated – Matthew Fellows, Joseph Barkate, and Dylan Eustice.

I would like to acknowledge Keysight Technologies for their cost-free loan of the Advanced Design Systems Software and Modelithics for their donation of simulation model libraries which were used in this research.

Finally, I would like to thank my family. I express my gratitude to my husband, Zachary Hays, for being a wonderful co-worker, filling my life with joy and laughter,

supporting and encouraging me, and being my best friend. I also sincerely thank my parents for being my first teachers and modeling the virtues of persistence, diligence, and most importantly selflessness to me. Thank you to my siblings – Katherine, Nicholas, Clare, and Anna – for all the love and laughter you've given me throughout my life. I am so blessed to have had all of you by my side for the adventure of graduate school.

ATTRIBUTIONS

Much of the work presented in this thesis has been published or presented and was made possible by collaboration with several colleagues. The contributions of the authors of [15, 33, 34, 37, 41] are detailed below.

In [15], a syndicated test bench for testing of reconfigurable circuit optimization algorithms was presented. This work is also presented as part of Chapter Two of this thesis. I developed the test bench at the Army Research Laboratory location with assistance from Viveiros. I also obtained the measurements using that bench, and compared the results from the two benches to verify syndication. Hays and Kappelmann developed the test bench at the Baylor University location and obtained measurements using that bench. The block diagram for the bench was first proposed by Baylis, who also contributed advice throughout the process. Marks, Penn, Hedden, and Darwish also offered general advice on load-pull measurements and circuit optimization. I authored the presentation and Baylis proofread the presentation.

In [33] and Chapter Three of this thesis, two algorithms using the tunable-varactor matching network were compared. I first proposed the idea of direct tuning of varactor bias voltages, obtained much of the data for both algorithms, and performed the comparison of the algorithms. Hays and Rezayat assisted in obtaining some of the data. Hays and Kappelmann set up the bench for obtaining the measurements. Walden and Egbert generated some figures based on the data. Fellows, Baylis, Marks, Viveiros,

Penn, Hedden, and Darwish offered general advice about the algorithms. I authored the publication and Baylis proofread the publication.

In [34] two methods of direct tuning of cavity position numbers of the evanescent mode cavity tuner for circuit optimization were presented. I developed the simplex method and obtained the data which is presented as part of Chapter Four of this thesis. Rezayat developed a modified gradient search method which was presented in [34] but is not included in this thesis. Peroulis, Abu-Khater, and Semnani designed and fabricated the evanescent mode cavity tuner. Baylis, Marks, and Viveiros offered general advice about the algorithms. Rezayat and I authored the presentation and Baylis proofread the presentation.

In [37] a new tool for broadband stability analysis with a design application was presented. This work is included as part of Chapter Five of this thesis. I developed the idea for the paper and obtained the data. Walden generated the Smith Tube figures for the paper. Baylis, Viveiros, and Marks offered general advice on stability analysis for amplifier design. I authored the publication and Baylis proofread the publication.

In [41] a new method of real time stability analysis using the acceleration of the gain was presented. This work is included as part of Chapter Five of this thesis. The idea for this method was first proposed by Baylis. I developed the specifics of the algorithm and obtained all of the simulation data. Egbert and I worked together to obtain the measurement data. Kappelmann performed the calculation of the input impedance. Marks and Viveiros offered general advice on stability analysis. I authored the presentation and Baylis proofread the presentation.

CHAPTER ONE

Introduction

For future radar systems to operate effectively, the systems must be designed with the ability to operate in an increasingly congested and contested spectrum. As more and more wireless devices are being introduced, available bandwidth has become in greater demand. As outlined by the National Broadband Plan of 2010, frequency bands previously used by radar have been and will continue to be reallocated to other wireless applications [1]. In some situations, radar systems also face contesting applications. As a result, the next generation radar must be cognitive, adaptive, and reconfigurable [2]. Cognitive radar systems are characterized by the ability to sense other wireless users in their environment, intelligently select an appropriate operating frequency and bandwidth, and reconfigure to operate efficiently under the conditions and constraints of the environment [3, 4]. The theory and foundation for cognitive radar have been discussed in the literature [2, 3, 4, 5]. However, many of these studies are theoretical in nature or focus primarily on signal processing solutions. Thus, there are still many microwave circuit technology challenges that must be addressed.

An important component of a reconfigurable radar system is the transmitter power-amplifier, since the power-amplifier directly affects the ability of the system to detect objects and maintain spectral compliance [6, 7, 8]. A reconfigurable power-amplifier requires a tunable matching network that can provide a variable load reflection coefficient to a transistor [9, 10]. The tunable matching network must be able to quickly

change operating conditions (notably, load reflection coefficient) to facilitate real time reconfiguration, have a wide enough bandwidth to support radar application, and be able to handle the large amounts of power outputted by the power-amplifier.

This thesis presents useful techniques for optimizing reconfigurable power-amplifiers using innovative tunable matching networks. Chapter Two introduces relevant power-amplifier concepts and the state-of-the-art in reconfigurable circuitry and stability analyses. Chapter Three presents a tunable-varactor matching network and discusses the differences between tuning the load reflection coefficient (Γ_L) and directly tuning the varactor bias voltages. Chapter Four overviews an innovative evanescent mode cavity tuner developed by Purdue University capable of handling up to 90 W of power. A gradient based load reflection coefficient optimization and a simplex based cavity position number optimization for power added efficiency (PAE) are presented. Chapter Five discusses methods for stability assessment in design and during reconfiguration of tunable power-amplifiers. Chapter Six presents some conclusions and suggestions for future work.

CHAPTER TWO

Background

The following sections provide background information which is useful for understanding the content of this thesis. The first section describes a graphical tool commonly used in Radio Frequency (RF) engineering known as the Smith Chart. The second section describes the function of power-amplifier matching networks and the role of the Smith Chart in designing these networks. The third section explains the power-amplifier load-pull process and key terms. The fourth section describes a syndicated test bench set up which was implemented in two locations for the purpose of joint collaboration of the algorithms presented in Chapters Three through Five. The fifth and sixth sections describe the state-of-the-art in reconfigurable power-amplifier design and power-amplifier stability analysis and design, respectively.

The Smith Chart

The Smith Chart is the two-dimensional graphical representation of the impedance mapped to the complex reflection coefficient plane and normalized to the characteristic impedance. The Smith Chart represents the relation

$$\Gamma = \frac{Z - Z_0}{Z + Z_0} \tag{1}$$

where Z_0 is the characteristic impedance. The Smith Chart can also be used to represent normalized admittance, but in this thesis, only the impedance Smith Chart is used. The Smith Chart is shown in Figure 2.1. The horizontal axis represents the real part of the

complex reflection coefficient Γ and the vertical axis represents the imaginary part of Γ. The circles that extend from the right side of the Smith Chart and are centered on the x axis represent constant resistance lines. The arcs that extend from the right side of the Smith Chart represent constant reactance lines. These are also circles, but only part of the circles is inside $|\Gamma| = 1$.

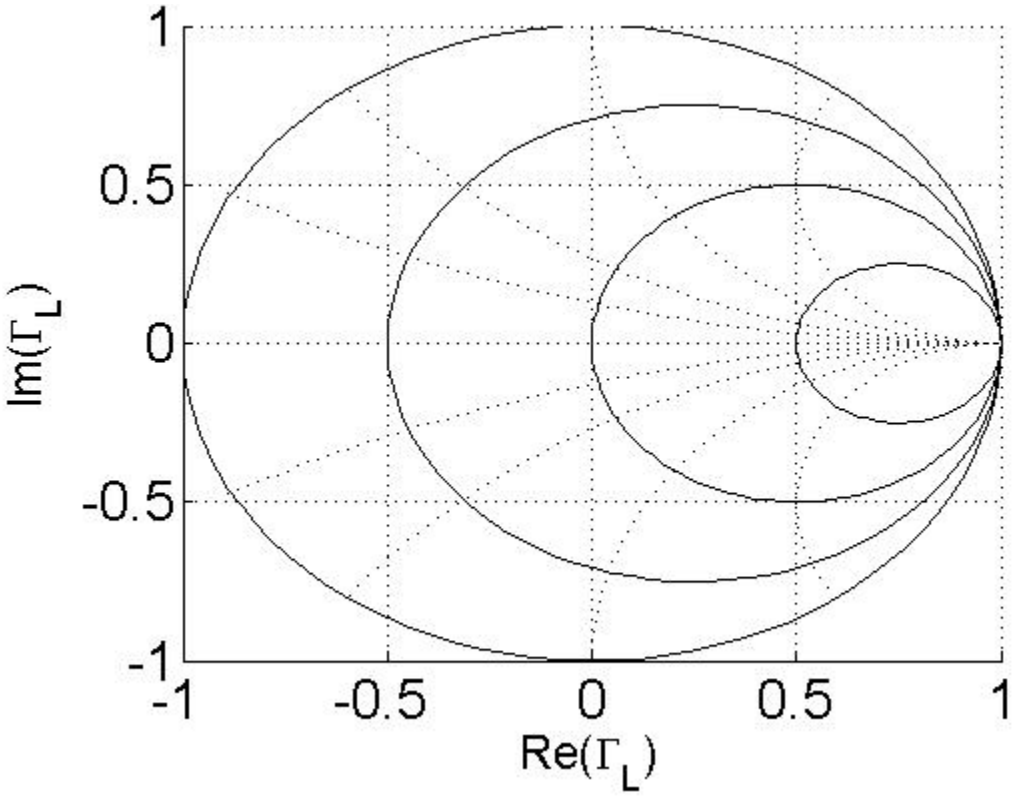

Figure 2.1 The Smith Chart

Power-Amplifier Impedance Matching

The performance of a power-amplifier is directly related to the load impedance, or load reflection coefficient, presented to it. Impedance matching is used in circuit design to present a desirable impedance to the power-amplifier device. Different values of load impedance can be selected to optimize gain, output power, efficiency, or linearity.

Spectral compliance is significantly related to the linearity of the amplifier. In traditional power-amplifiers, a matching network can be designed with reactive components or transmission-line sections with fixed lengths to achieve the desired performance. Since capacitances, inductances, and line lengths can be represented by arcs on the Smith Chart, the Smith Chart is a useful tool for determining the circuitry needed to match one impedance to another.

In a reconfigurable power-amplifier, changing transistor parameters and varying performance requirements, such as operating frequency, efficiency, and linearity, means that the optimum load reflection coefficient of the amplifier ranges accordingly, requiring tunable matching networks. Designing reconfigurable matching networks with tunable circuitry is an important area of recent research [6, 9, 11, 12, 13, 14]. The work done in this thesis describes algorithms designed to optimize amplifier performance with reconfigurable matching on the load side of the amplifier. However, it is expected that the algorithms demonstrated can also be applied to reconfigurable source impedance matching. In this thesis, optimization using two different reconfigurable matching networks are studied. The first is implemented using a circuit of varactor diodes and the second is a high-power matching network that uses tunable resonant cavities to provide a variety of load reflection coefficients for the reconfigurable power-amplifier. Many of the tuning methods discussed in this thesis are applicable to other reconfigurable matching networks as well.

Load-Pull Key Terms

A load-pull measurement allows examination of amplifier device performance variation with load reflection coefficient. In a load-pull measurement, a variety of load

reflection coefficients are presented to the transistor, and at each state, performance metrics are measured. These metrics are then plotted as contours on the Smith Chart to provide a visual representation of the amplifier performance with respect to load reflection coefficient. Power-added efficiency (PAE) and adjacent-channel power ratio (ACPR) are two metrics used to assess the performance of a power-amplifier. The PAE of an amplifier measures how much of the input power is converted to output power. High PAE is desirable for power-amplifiers. The PAE is defined as follows:

$$PAE = \frac{P_{out,RF} - P_{in,RF}}{P_{DC}} \times 100\% \quad (2)$$

ACPR measures the ratio of the power of a signal in a defined adjacent channel to the power in the main channel. A low ACPR is desirable for power-amplifiers. High ACPR conveys that significant spectral spreading is occurring due to nonlinearities in the power-amplifier.

An example of PAE and ACPR contours for a Microwave Technologies MWT-173 GaAs field effect transistor (FET) biased at $V_{DS} = 4.5\ V$ and $V_{GS} = -1.5\ V$ with an input power of 14 dBm and a 3.3 GHz signal is shown in Figure 2.2. As seen in the figure, there is often a trade-off to be made between a high PAE and a low ACPR. In the algorithms presented in this thesis, an ACPR limit is set and the load reflection coefficient is optimized to achieve the highest PAE within the ACPR constraint.

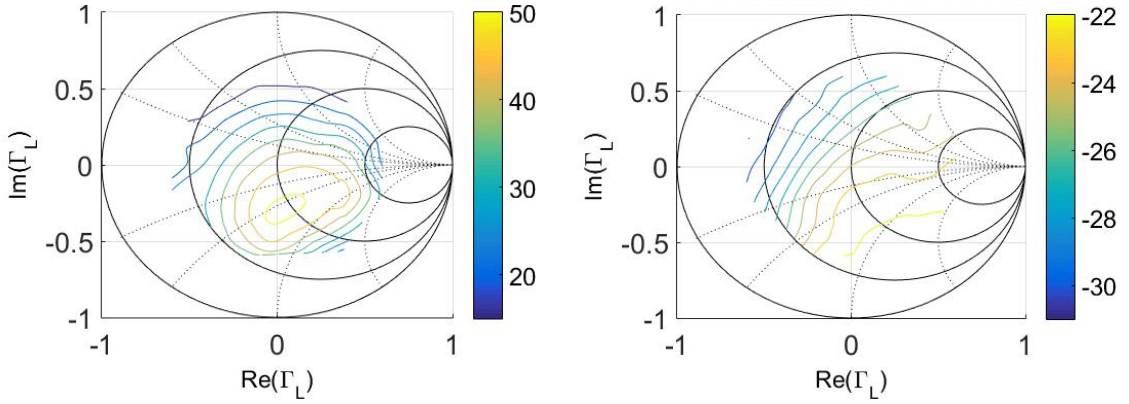

Figure 2.2 Example transistor PAE (left) and ACPR (right) contours. The device under test is a Microwave Technologies MWT-173 GaAs field effect transistor (FET) biased at $V_{DS} = 4.5\ V$ and $V_{GS} = -1.5\ V$ with an input power of 14 dBm and a 3.3 GHz signal.

Syndicated Test Bench Set Up

This section has been presented as: [15] Lamers, L.; Hays, Z.; Kappellmann, C.; Baylis, C.; Marks, R.; Viveiros, E.; Penn, J.; Hedden, A.; Darwish, A, "Syndicated Test Bench Set-up for Testing of Real-time Reconfigurable Power-amplifiers for the Next Generation Radar." USNC-URSI National Radio Science Meeting, January 2017, Boulder, Colorado.

The algorithms presented in this thesis were developed under a collaborative effort with the Army Research Laboratory for research on the next generation radar. In order to facilitate collaboration, a syndicated test bench was developed for designing and testing algorithms at two locations. The test bench was first developed at Baylor University and then imitated as closely as possible by the author at the Army Research Laboratory using the available equipment. The test benches were designed to use the tunable-varactor matching network and were later modified to include the ability to use the tunable resonant cavity network. Figure 2.3 shows the block diagram of the measurement set up. Figures 2.4 and 2.5 show the test bench implemented with available equipment in both locations.

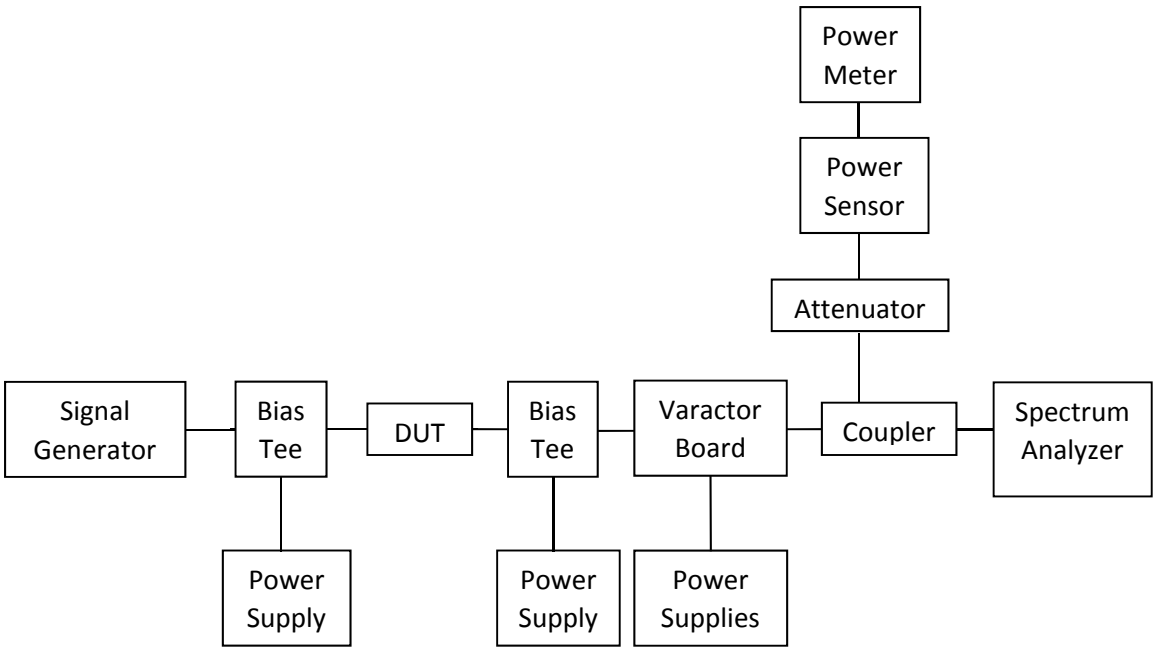

Figure 2.3 Syndicated test bench set-up

Figure 2.4 Test bench at Baylor University

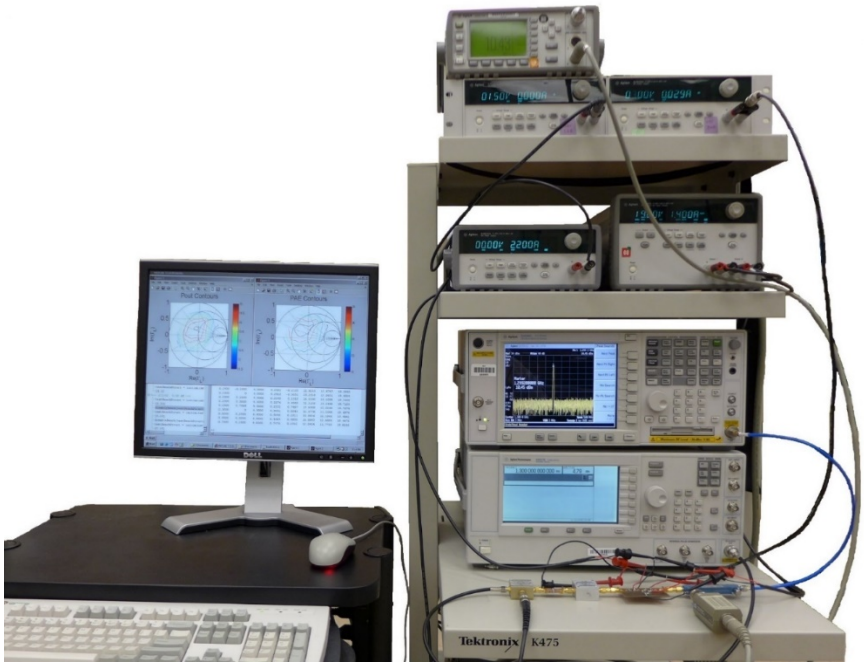

Figure 2.5 Test bench at the Army Research Laboratory

In order to verify that the two benches were indeed syndicated, a load-pull measurement of a device and a load reflection coefficient optimization for device output power was performed at each location. A Microwave Technologies MWT-173 GaAs field-effect transistor (FET) was used as the transistor under test. Although the same model of transistor was used in both locations, two different physical devices were measured. Thus the results are acceptably comparable but not identical. The results of the output-power load-pull for both devices are shown in Figure 2.6. The results of an example optimization are shown in Figure 2.7 and a summary of several optimizations starting at different load reflection coefficients is shown in Table 2.1. Bench syndication is evidenced by the similarity in the device contours and optimization results.

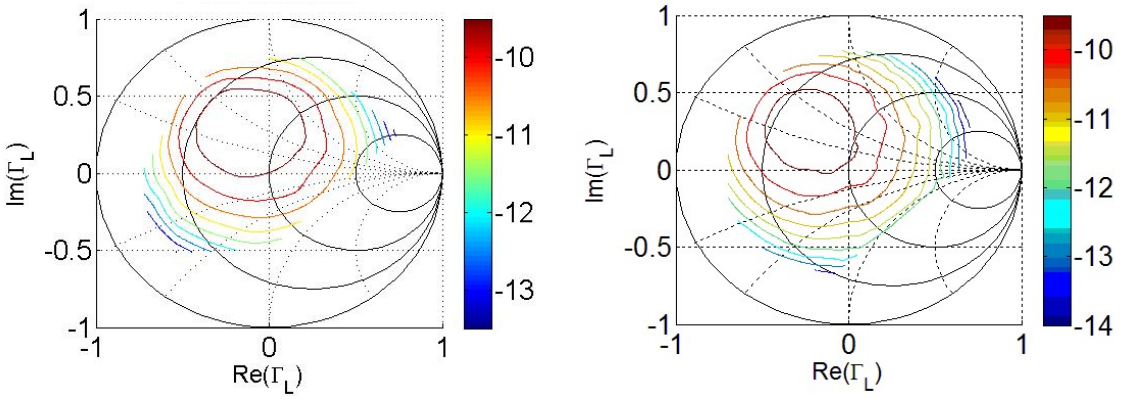

Figure 2.6 Output power load-pull contours compared for the Army Research Laboratory test bench (left) and the Baylor University test bench (right). The device under test is a Microwave Technologies MWT-173 GaAs field effect transistor (FET) biased at $V_{DS} = 4.5\ V$ and $V_{GS} = -1.5\ V$ with an input power of -20 dBm and a 3.3 GHz signal.

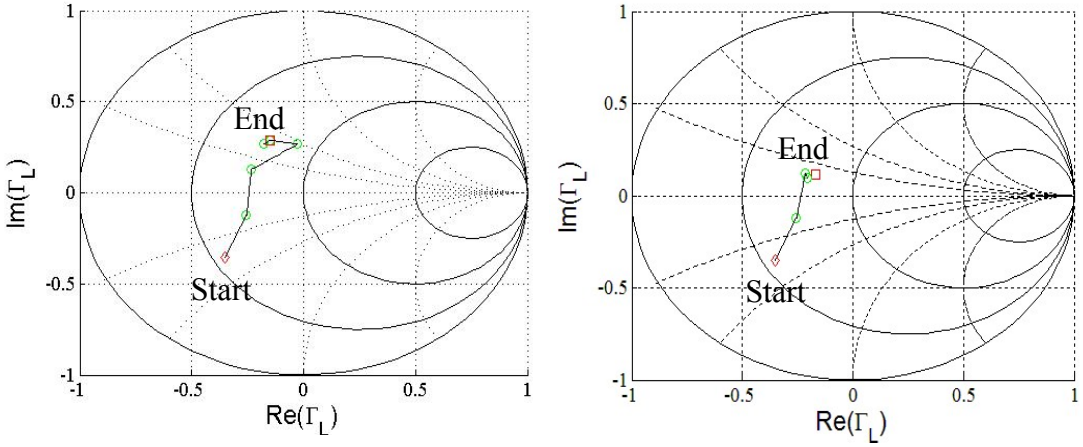

Figure 2.7 Example optimization starting at $\Gamma_L = 0.5\angle -135°$ performed using the Army Research Laboratory test bench (right) and the Baylor University test bench (left). The device under test is a Microwave Technologies MWT-173 GaAs field effect transistor (FET) biased at $V_{DS} = 4.5\ V$ and $V_{GS} = -1.5\ V$ with an input power of -20 dBm and a 3.3 GHz signal. Using the Army Research Laboratory test bench, optimum output power was found at $\Gamma_L = 0.3257\angle 117.5504°$. The search ended after 20 measurements with a final output power of -9.0567 dBm. Using the Baylor University test bench, optimum output power was found at $\Gamma_L = 0.2043\angle 145.0591°$. The search ended after 13 measurements with a final output power of -9.1366 dBm.

Table 2.1 Comparison of several optimizations performed on the Army Research Laboratory test bench and the Baylor University test bench from various starting locations. The device under test is a Microwave Technologies MWT-173 GaAs field effect transistor (FET) biased at $V_{DS} = 4.5\ V$ and $V_{GS} = -1.5\ V$ with an input power of -20 dBm and a 3.3 GHz signal.

Start Γ_L	**End Γ_L (ARL)**	**End Γ_L (Baylor)**	**End Pout dBm (ARL)**	**End Pout dBm (Baylor)**	**Number of Meas. (ARL)**	**Number of Meas. (Baylor)**
0.5∠90°	0.25∠115.62°	0.44∠147.33°	-9.00	-9.16	10	13
0.5∠135°	0.45∠105.57°	0.30∠143.05°	-9.06	-9.04	18	10
0.5∠-90°	0.35∠119.34°	0.39∠115.02°	-8.99	-9.03	27	19
0.5∠-135°	0.33∠117.55°	0.20∠145.06°	-9.05	-9.14	20	13
0.25∠45°	0.30∠104.32°	0.32∠137.09°	-9.00	-9.08	13	25
0.25∠135°	0.36∠119.38°	0.29∠128.48°	-9.00	-9.01	20	18
0.25∠-45°	0.29∠119.56°	0.40∠117.07°	-9.01	-9.03	23	19
0.25∠-135°	0.34∠105.74°	0.43∠138.07°	-9.00	-9.08	17	13
		Average	**-9.01**	**-9.08**	**18.5**	**16.7**

The main purpose of the syndicated test bench set up was to facilitate collaboration on the project leading to joint innovation. Other advantages include the ability to test a greater variety and number of devices and expand algorithm operation to higher frequencies due to the additional availability of devices and equipment at a second location.

State-of-the-Art in Reconfigurable Power-amplifiers

Achieving amplifier reconfigurability requires an intelligent method of load reflection coefficient optimization using a tunable matching network [9, 10]. In the literature, most algorithms focus on optimizing the gain, output power, or PAE of the power-amplifier using a tunable matching network [6, 11, 12, 13]. These methods do not consider the spectrum compliance in the optimization algorithms.

Several algorithms for tuning the load reflection coefficient of an amplifier to optimize PAE while maintaining spectral compliance have been presented [16, 17, 18,

19, 20]. In these algorithms, the PAE and ACPR gradients are estimated, as illustrated in Figure 2.8, to determine the direction of travel on the Smith Chart.

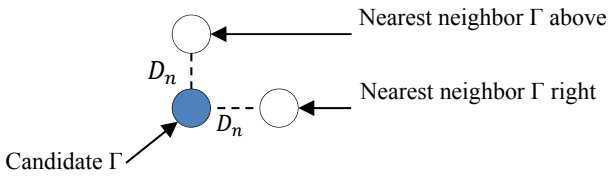

Figure 2.8 Two neighboring points are measured at each candidate point for estimating the circuit PAE and ACPR gradients, reprinted from [16].

The process and equations that follow were first published in [16]. For every candidate Γ in the search, two neighboring points separated by a distance D_n on the Smith Chart are used to estimate the PAE and ACPR gradients. Then, the optimal directions of travel for PAE, given by unit vector $\hat{p}$, and ACPR, given by unit vector $\hat{a}$ are calculated. These vectors are related to the gradients ∇p and ∇a as follows:

$$\hat{p} = \frac{\nabla p}{|\nabla p|} \tag{3}$$

$$\hat{a} = -\frac{\nabla a}{|\nabla a|} \tag{4}$$

The equation for $\hat{a}$ contains a negative sign because decreasing ACPR represents the optimal direction of travel.

The next step in the search is chosen as illustrated in Figure 2.9. If the ACPR of the current candidate point is unacceptable, or greater than the specified limit, then the search vector is given by

$$\bar{v} = \hat{a}D_a + \hat{b}D_b, \tag{5}$$

where $\hat{b}$ is a unit bisector of $\hat{a}$ and $\hat{p}$. If the ACPR of the current candidate point is acceptable, it is less than the limiting value (acceptable) at the present candidate, and the search vector is instead given by

$$\bar{v} = \hat{p}D_a + \hat{b}D_b. \tag{6}$$

In these equations

$$D_a = \frac{D_s}{2}\frac{|ACPR_{cand} - ACPR_{limit}|}{|ACPR_{worst} - ACPR_{limit}|}, \tag{7}$$

$$D_b = \frac{D_s}{2}\frac{|\theta_{cand} - 90°|}{90°}. \tag{8}$$

$ACPR_{cand}$ is the ACPR value in dBc at the candidate point, $ACPR_{limit}$ is the ACPR constraint value in dBc, and θ_{cand} is the value of the angle between $\hat{a}$ and $\hat{b}$ at the candidate point.

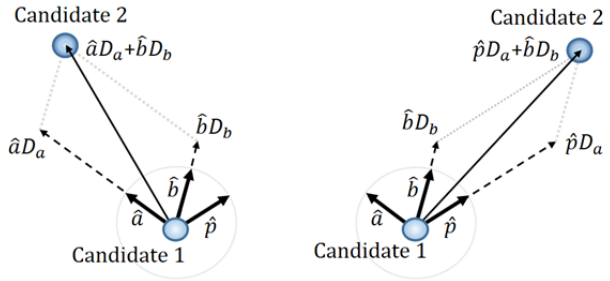

Figure 2.9 Method for finding the next candidate point if the ACPR of the current candidate point is unacceptable (left) or acceptable (right), reprinted from [16].

In addition to an intelligent algorithm, another component necessary for achieving amplifier reconfigurability is a tunable matching network. The speed of the algorithm described above is largely dependent on the speed of reconfiguration of the tunable matching network. In the literature, microelectromechanical systems (MEMS) switches are shown to provide excellent speed and tunability for reconfigurable circuitry [6, 11].

However, most MEMS devices are not capable of handling the power necessary for radar transmitter power-amplifiers. For cognitive or adaptive radar systems, the tunable matching network must be able to handle the high input powers characteristic of radar systems. In [16, 17, 18, 19, 20], a commercially available bench measurement tuner from Maury Microwave is used as the tunable matching network. While this tuner and similar commercially available bench measurement tuners are quite accurate and have excellent tuning range, they are too large and slow to be practical for use in real-time reconfigurable radar systems. In [9, 14] a circuit of varactor diodes is shown to have decent tuning range and to perform much more quickly than a mechanical load impedance tuner. However, this technology does not have the power handling capability necessary for radar systems. Developing high-power tunable devices has been an area of interest in recent years [21, 22, 23, 24]. For example, a tunable evanescent-mode resonant cavity tuner has been designed and fabricated which provides the ability to adjust load reflection coefficient while handling up to 90 W of power [21]. The device has a control loop which utilizes a feedback cavity stacked on top of the resonant cavity to monitor and maintain stability [25]. A similar device uses an evanescent-mode resonant cavity capable of handling high power in a tunable microwave filter and tunable diplexer [23, 24]. Further refinements of this technology may include an implementation using plasma devices for even higher power handling [22].

State-of-the-Art in Power-Amplifier Stability Analysis and Design

In a first design pass, amplifiers are typically designed to be stable by analyzing the circuit only at the design frequency under small-signal inputs. Under small-signal stimulation, reflection coefficients that result in potentially unstable transistor operation

plot to a stability circle. If the stability circle intersects the Smith Chart, the device is potentially unstable. Figure 2.10 depicts the stability circle for a simulated Modelithics model of a Qorvo TGF 2960 pseudomorphic high electron mobility transistor (pHEMT). performed under small-signal excitation at 2 GHz with bias $V_{DS} = 5\ V$ and $V_{GS} = -1\ V$ as an example of a potentially unstable device. If the stability circle lies completely outside of the Smith Chart, the device is said to be unconditionally stable at the design frequency for small-signal inputs. In a typical amplifier design process, stability and gain circles are plotted using the small-signal S-parameters at the design frequency [26]. If unconditional stability for small-signal inputs is desired, the designer may add a stabilizing resistor at the input or output of the device to push the stability circle outside of the Smith Chart. Next, the input and output matching networks are designed [26]. Once the amplifier is designed, geometrically derived stability factors can be measured to analyze stability for small-signal inputs over a range of frequencies [27].

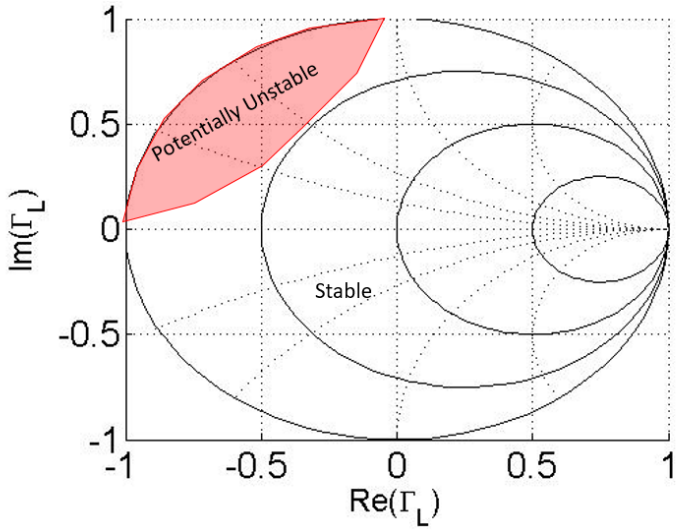

Figure 2.10 Example load stability circle showing regions of unconditionally stable and potentially unstable load reflection coefficients. Device is a Modelithics model of a Qorvo TGF 2960 pseudomorphic high electron mobility transistor (pHEMT). Performed under small-signal excitation at 2 GHz with bias $V_{DS} = 5\ V$ and $V_{GS} = -1\ V$.

While small-signal stability analysis has been well developed, large-signal stability analysis is more complex. Suarez presents stability problems that arise in the large-signal regime, including spurious oscillations and frequency divisions [28]. Methods for analyzing stability under large-signal inputs include characterizing the circuit with differential equations and using Floquet theory [29, 30, 31, 32]. These methods are typically time-consuming and computationally heavy.

CHAPTER THREE

Tuning with the Tunable-Varactor Matching Network

Information in this chapter has been published as: [33] Lamers, L.; Hays, Z.; Kappelmann, C.; Rezayat, S.; Fellows, M.; Walden, E.; Egbert, A.; Baylis, C.; Marks, R.; Viveiros, E.; Penn, J.; Hedden, A.; Darwish, A., "Comparison of Bias-voltage and Reflection-coefficient Based Reconfiguration of a Tunable-varactor Matching Network for Adaptive Amplifiers." 2017 IEEE 18th Wireless and Microwave Technology Conference (WAMICON), Cocoa Beach, FL, 2017.

The gradient based constrained PAE optimization presented in Chapter Two was designed using a commercially available bench measurement load-pull tuner from Maury Microwave as the tunable matching network. However, the Maury load-pull tuner is not a practical solution for implementation in the field, as small devices capable of very fast tuning are needed. Therefore, a tunable-varactor matching network following the design of [9] was constructed. The tunable-varactor matching network is also not useful in the field due to power limitations, but it reveals some non-idealities that will need to be dealt with in using reconfigurable circuitry. The tunable-varactor matching network consists of three varactor diodes. Figure 3.1 shows the design of the matching network.

The capacitance of each varactor diode is controlled by setting the bias voltage, effectively changing the load reflection coefficient of the matching network. V_1, V_2, and V_3 are defined as the bias voltages applied to each varactor at the locations shown in Figure 3.1. Changing one bias voltage at a time moves the load reflection coefficient of the device along an arc on the Smith Chart, as shown in Figure 3.2. Transistor output power load-pull contours are also depicted, showing how output power varies as bias

voltage changes. With three bias voltages to control, the matching network can reach values of load reflection coefficient (Γ_L) across a significant portion of the Smith Chart.

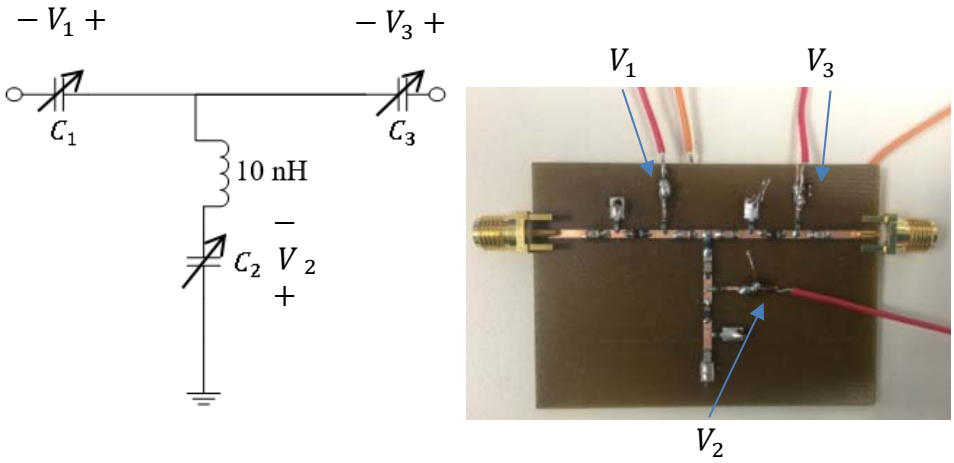

Figure 3.1 Simplified circuit schematic (left) and fabricated tunable-varactor matching network (right)

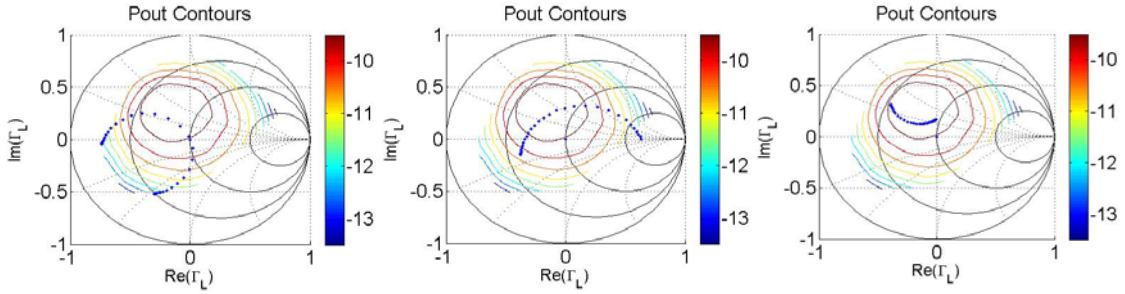

Figure 3.2 Load reflection coefficients obtained by holding two bias voltages constant and varying the remaining bias voltage from 0 V to 30 V in steps of 1 V.

Figure 3.3 shows the measured tuning range of the matching network. The figure was generated by performing a characterization of the device. The characterization was performed by setting the bias voltages of the varactors to different combinations of V_1, V_2, and V_3 and recording the corresponding load reflection coefficient obtained for each voltage setting.

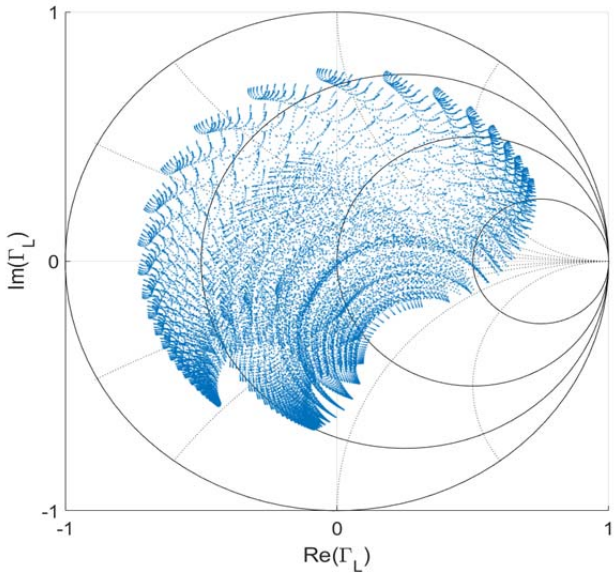

Figure 3.3 Tuning range of the tunable-varactor matching network

The load reflection coefficient optimization discussed in Chapter Two can be implemented using the tunable-varactor matching network as the reconfigurable load matching network. Since the algorithm uses Γ_L as the optimization parameter, but the bias voltages are actually the fundamental tuning elements of the matching network, an additional step is needed during each measurement: using a look-up table which relates voltage setting to Γ_L. From this, the search algorithm can identify the characterized Γ_L point nearest to the point needed and the voltage setting that generates that point must be determined.

Comparison of Γ_L Tuning and Direct Bias Voltage Tuning

The algorithm for the Γ_L optimization was implemented using the tunable-varactor matching network. It was found that the look-up table added about an additional second per measurement to the optimization, which is undesirable for a real-time reconfigurable radar system [33].

In order to bypass the look-up table, the bias voltages can be directly tuned in a three dimensional search space. A gradient based approach, similar to the process used in the Γ_L optimization, can be used. The gradient estimation approach is shown in Figure 3.4. Since the network has three tuning elements, the voltage based search is performed in a three dimensional search space.

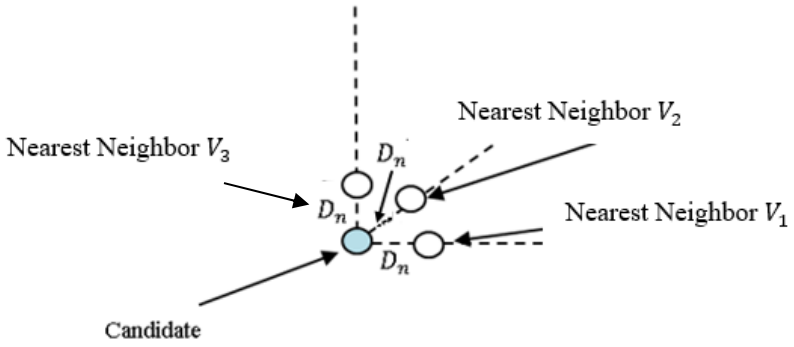

Figure 3.4 Neighboring points used in the bias voltage search space to construct search vectors.

As in the two dimensional reflection coefficient search space described in Chapter Two and first presented in [16], the search vectors are constructed based on unit vectors in the direction of increasing PAE ($\hat{p}$) and decreasing ACPR ($\hat{a}$). The unit vector $\hat{b}$ bisects vectors $\hat{p}$ and $\hat{a}$. If the ACPR at the candidate is greater than the specified ACPR constraint, than the search vector identifies the next candidate as:

$$\overline{v} = \hat{a}D_a + \hat{b}D_b \tag{9}$$

where

$$D_a = \frac{D_S}{2}\frac{|ACPR_{meas} - ACPR_{target}|}{|ACPR_{worst} - ACPR_{target}|}, \tag{10}$$

and

$$D_b = \frac{D_s}{2}\frac{|\theta_{meas} - \theta_{target}|}{\theta_{target}}. \quad (11)$$

Then, the process for determining the next candidate in the three dimensional bias voltage space is shown in Figure 3.5.

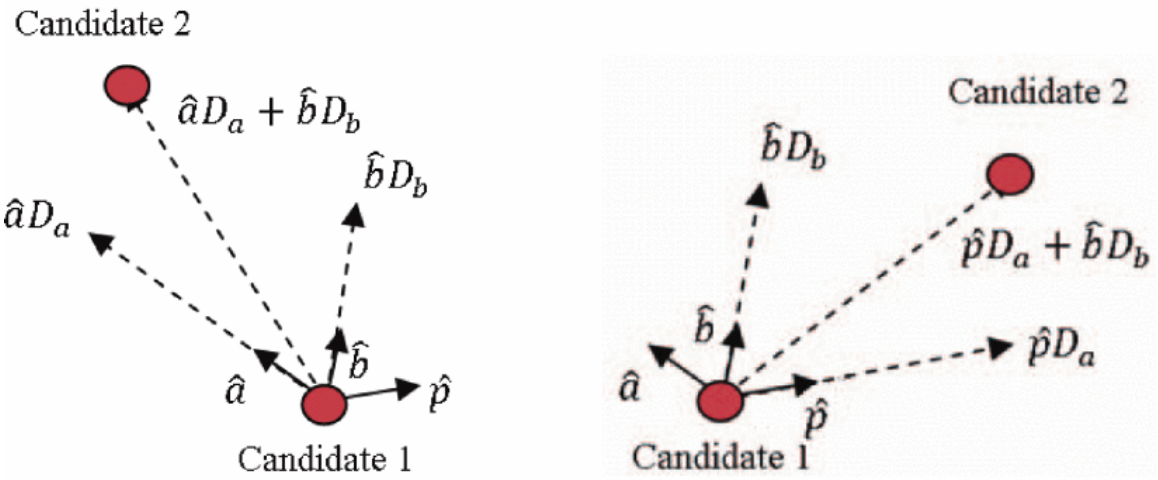

Figure 3.5 Process for choosing the next candidate in the search if ACPR is out of compliance (left) or if ACPR is in compliance (right) [16].

The two different optimizations were compared based on their performance in matching a Microwave Technologies MWT-173 FET. The device operated at a bias of $V_{GS} = -1.5\ V$ and $V_{DS} = 3\ V$ with input power $P_{in} = 4\ dBm$. $ACPR \leq -30.5\ dBc$ was used as the ACPR constraint. Each optimization process was shown to have advantages and disadvantages. PAE contours for each search space are shown in Figure 3.6. Several search ending locations are shown overlaid on the contours.

Typical power-amplifier PAE contours form ovals in the Smith Chart. The contours in Figure 3.6 are not circular because the tunable-varactor matching network is measured as part of the device under test. The reference plane is located between the matching network and the power meter. In other words, the PAE is measured at the

output of the matching network rather than at the output of the amplifier before the matching network. This set up also means that lower PAE values are reported because the matching network introduces some loss. The tunable-varactor matching network is included as part of the device under test so that the Γ_L optimization can be directly compared to the bias voltage optimization. In a standard Γ_L optimization or load-pull measurement the PAE is reported at the output of the amplifier. The power is first measured at the output of the matching network and then the S-parameters of the matching network are used to calculate the matching network loss which is then added to the measured power to obtain the value at the output of the amplifier. A characterization of the S-parameters of the matching network is needed for this process. However, in the bias voltage optimization, a device characterization is not used, so the S-parameters of the matching network are not available, meaning that the PAE must be measured at the output of the matching network. Furthermore, in a radar system, the overall power sent to the transmitter matters more than the power measured at the output of the power-amplifier, so it is reasonable to take matching network loss into consideration during the optimization. The reference plane for the contours shown above and used in the algorithms compared to the reference plane for standard load-pull measurements are shown in Figure 3.7.

Even though the contours are not circular when considering the matching network as part of the device under test, the PAE contours in the Smith Chart are more friendly for the gradient optimization. In the three-dimensional bias voltage space, the contours are non-convex and there are two local optima. This is because different combinations of bias voltages can map to very similar load reflection coefficients. In addition, a third

neighboring point measurement is needed in the bias voltage search because it is a three-dimensional space rather than a two-dimensional space. However, extra time is needed for the Γ_L optimization due to the look up table. Also, the only points that can be reached in the Γ_L optimization are the characterized points. Interpolating between points is not feasible as changing bias voltage translates to moving in an arc, not a line, on the Smith Chart and equal steps in bias voltage do not correspond to moving equal distances on the Smith Chart.

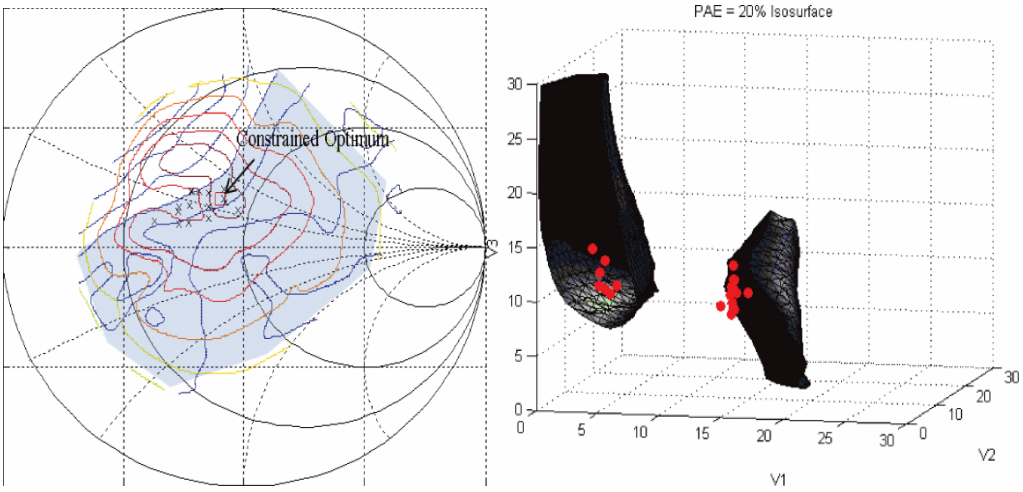

Figure 3.6 PAE contours for the Γ_L search space (left) and an equal PAE surface in the bias voltage search space (right). The black x's on the figure in the left and the red dots in the figure on the right depict search ending locations. In the bias voltage space, the search end locations form two clusters, meaning the search space is multi-modal.

Figure 3.8 compares an example search trajectory in each search space. In both cases, the search converged at an acceptable point. More measurements were required in the three dimensional bias voltage search space, but the time per measurement was less. Table 3.1 presents the results of the gradient optimization in the Γ_L search space, Table 3.2 presents the results of the gradient optimization in the bias voltage search space, and Table 3.3 provides a comparison of the two methods.

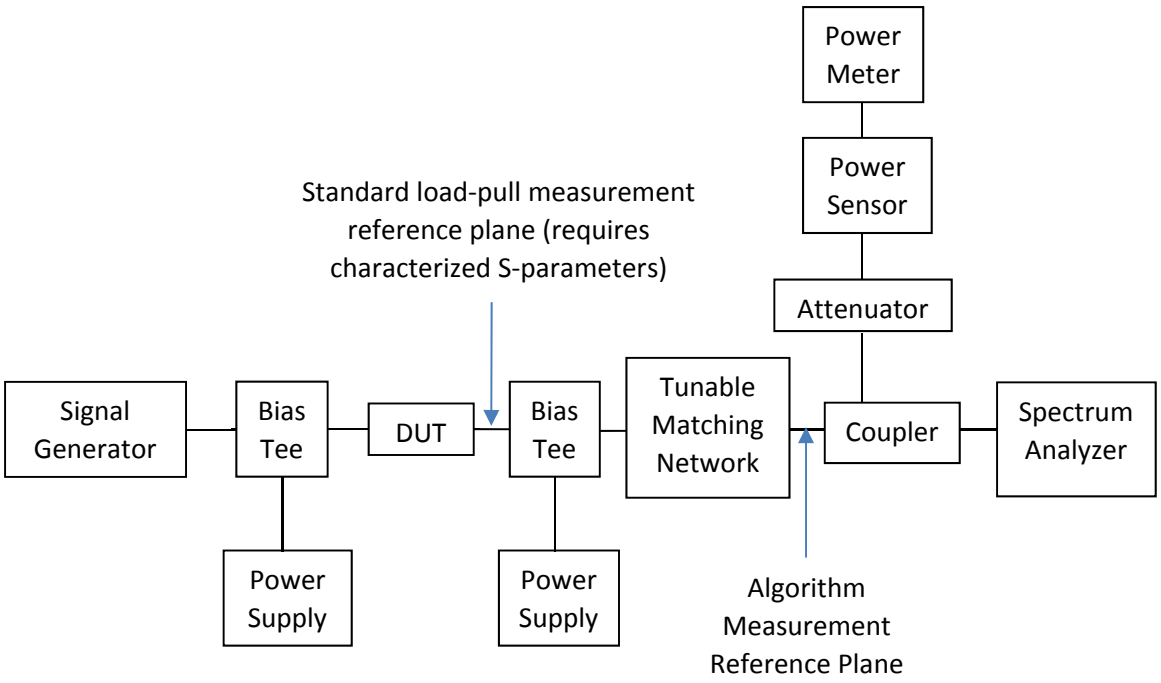

Figure 3.7 The reference plane for the contours shown above and used in the algorithms compared to the reference plane for standard load-pull measurements

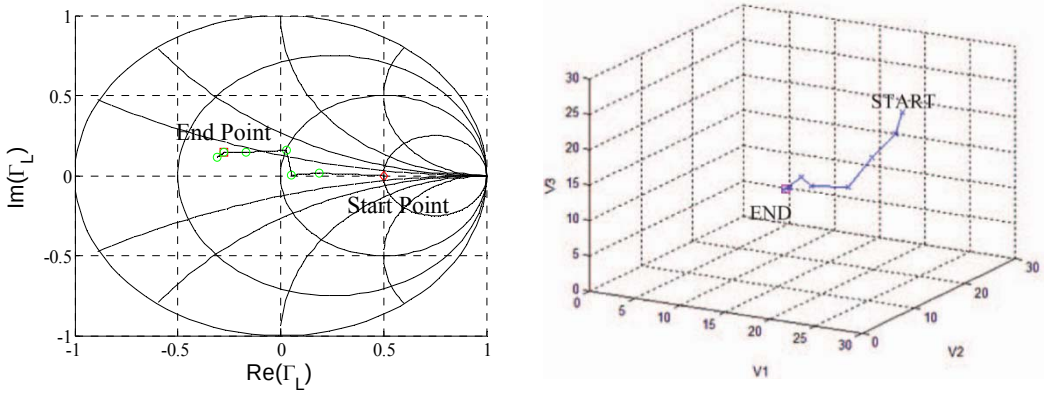

Figure 3.8 Reflection-coefficient search results for starting point $\Gamma_L = 0.50/\underline{0°}$ (left). The constrained optimum was found at $\Gamma_L = 0.31/\underline{151.84°}$, providing PAE = 27.73% and ACPR = -30.61 dBc. 26 measurements were required, with an average time per measurement of 3.63 seconds. Bias voltage search results for starting point $V_1 = 22\ V, V_2 = 22\ V, V_3 = 22\ V$ (right). The constrained optimum was found at $V_1 = 12.11\ V, V_2 = 16.80\ V, V_3 = 10.93\ V$, providing PAE = 26.02% and ACPR = −30.97 dbc. 32 measurements were required, with an average time per measurement of 2.58 seconds.

As seen in Table 3.1, from several starting locations, the reflection coefficient search consistently converged to an ending location that met the ACPR constraint and provided about 27% PAE with an average of 21.13 measurements. Much of the time per measurement is due to equipment control overhead, but a significant portion is due to increased computation time using the look-up table.

Table 3.1 Results of the gradient optimization in the Γ_L search space

Start Γ_L	Start PAE (%)	End Γ_L	End ACPR (dBc)	End PAE (%)	# Meas.	Avg. time per meas. (sec.)
0/0°	21.24	0.19/139°	-31.0	26.87	11	3.41
0.25/0°	13.79	0.28/143°	-30.8	28.40	21	3.39
0.25/45°	20.10	0.33/133°	-30.6	29.31	23	3.39
0.25/90°	22.74	0.39/164°	-30.5	25.61	12	3.43
0.25/-45°	12.40	0.25/110°	-31.4	27.67	21	3.50
0.25/-90°	12.39	0.32/148°	-31.1	27.68	34	3.41
0.25/135°	26.76	0.22/112°	-31.0	27.10	16	3.54
0.25/180°	23.80	0.29/160°	-31.6	26.85	13	3.39
0.25/-135	16.61	0.22/131°	-30.8	26.71	14	4.28
0.5/0°	6.94	0.31/152°	-30.6	27.73	26	3.63
0.5/45°	8.28	0.21/112°	-31.4	26.31	30	3.40
0.5/90°	12.79	0.27/122°	-30.9	28.47	27	3.48
0.5/-135°	9.22	0.25/156°	-31.1	25.69	24	3.42
0.5/-90°	5.27	0.16/98°	-31.8	24.53	20	3.40
0.5/135°	22.18	0.30/129°	-30.6	28.91	17	3.53
0.5/180°	9.91	0.32/132°	-30.5	28.95	29	3.48
		Average	**-30.99**	**27.30**	**21.13**	**3.50**

As seen in Table 3.2, from several starting locations in the three dimensional bias voltage space, the search consistently converged to an ending location that met the ACPR constraint and had a PAE of about 27% in an average of 35.85 measurements. The increase in the average number of measurements compared to the reflection coefficient search space optimization is due to the fact that the search space is three dimensional, so a third neighboring point measurement is needed at each candidate point in the search. If only two bias voltages were used as tuning elements, the search space would be two

dimensional, which could make the number of measurements for direct tuning of the fundamental tuning elements more comparable to tuning the load reflection coefficient. A notable advantage of tuning the bias voltages directly is that the time per measurement is significantly less than the reflection coefficient search space optimization.

Table 3.2 Results of the gradient optimization in the bias voltage search space

Start V_1 (V)	Start V_2 (V)	Start V_3 (V)	Final V_1 (V)	Final V_2 (V)	Final V_3 (V)	End PAE (%)	End ACPR (dBc)	# Meas.	Avg. time per meas. (sec.)
1	1	1	5.15	1.70	13.68	28.35	-31.11	16	2.46
2	2	2	5.52	0.11	11.34	27.99	-31.26	29	2.47
3	3	3	5.78	2.98	11.20	27.04	-31.36	20	2.52
4	4	4	4.79	1.55	12.60	28.55	-31.01	25	2.46
5	5	5	5.75	1.01	10.74	27.93	-31.46	25	2.53
6	6	6	4.57	0.00	15.07	29.63	-30.53	19	2.46
7	7	7	5.06	0.18	11.66	28.14	-31.06	52	2.50
8	8	8	5.34	0.64	13.89	27.23	-31.11	34	2.48
9	9	9	12.53	14.10	6.98	26.94	-30.53	25	2.49
10	10	10	12.65	14.73	7.26	26.95	-30.80	29	2.50
11	11	11	12.34	15.74	9.01	26.46	-30.59	40	2.50
12	12	12	12.09	15.62	8.45	26.90	-30.52	33	2.49
13	13	13	12.23	16.05	9.76	26.98	-30.75	81	2.46
14	14	14	12.65	15.55	8.63	26.63	-30.98	53	2.47
15	15	15	11.52	14.68	7.60	26.60	-30.91	25	2.47
16	16	16	12.36	15.30	7.78	26.93	-30.54	53	2.47
17	17	17	13.54	15.69	8.64	25.85	-30.84	16	2.47
18	18	18	12.28	16.23	9.70	26.02	-30.79	41	2.46
					Average	**27.22**	**-30.88**	**35.85**	**2.48**

In conclusion and as seen in Table 3.3, both methods can be used for optimization of power-amplifier PAE within an ACPR constraint. Even though the search space is three dimensional and multi modal for the bias voltage search, optimum PAE and ACPR are comparable to the Γ_L search. Therefore, the bias voltage search provides the

advantages of time savings per measurement and simpler implementation by removing the need for the characterization process and look up table.

Table 3.3 Comparison of the bias voltage and reflection coefficient search results

		End ACPR (dBc)	End PAE (%)	Avg. # Meas.	Avg. Time per Meas. (sec.)	Avg. Time per Search (sec.)
Γ_L Search	Average	-30.99	27.30	21.13	3.50	73.70
	Standard Deviation	0.39	1.31	6.73	0.21	22.65
Voltage Search	Average	-30.88	27.22	35.85	2.48	88.97
	Standard Deviation	0.27	0.96	17.81	0.03	43.77

CHAPTER FOUR

Tuning with the Evanescent Mode Cavity Tuner

Information in this chapter has been presented as [34] Hays, L.; Rezayat, S.; Baylis, C.; Marks II, R.; Viveiros, E.; Peroulis, D.; Abu-Khater, M.; Semnani, A.; "Direct Tuning of Cavity Position Numbers for Circuit Optimization Using an Evanescent-Mode Cavity Tuner Designed for Reconfigurable Radar Transmitters" USNC-URSI National Radio Science Meeting, January 2018, Boulder, Colorado

A second reconfigurable matching network has been designed and fabricated by a group at Purdue University [21]. The specifications for the center frequency, bandwidth, and power handling capabilities of the tuner were requested by Dr. Baylis and then the authors of [21] independently designed and fabricated the tuner. The design of the tuner is shown in Figure 4.1 and the fabricated tuner is shown in Figure 4.2. This matching network consists of two evanescent mode resonant cavities. The resonant frequency of each cavity is varied through control of the length of the cavity, which is set by controlling the height of a piezoelectric disk. Varying the resonant frequency of the two tuning elements allows the user to adjust the load reflection coefficient of the tuner presented to the amplifier. The fundamental tuning element that is input to the tuner is the combination of two resonant cavity position numbers (n_1 and n_2). The evanescent mode cavity tuner is capable of handling 90 W of power and has a bandwidth on the order of 30%. It also has increased coverage of the Smith Chart compared to the tunable-varactor matching network.

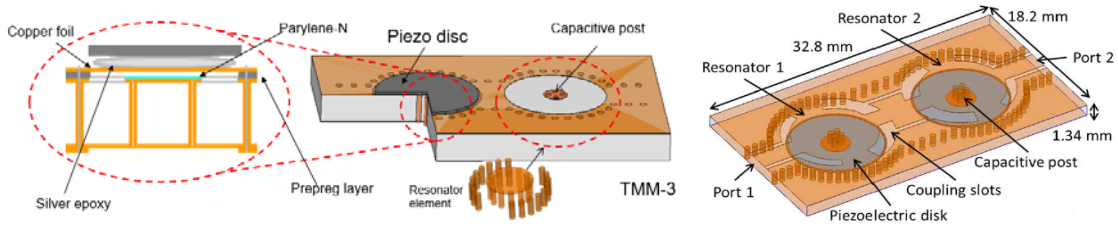

Figure 4.1 Design of the evanescent mode cavity tuner [21]

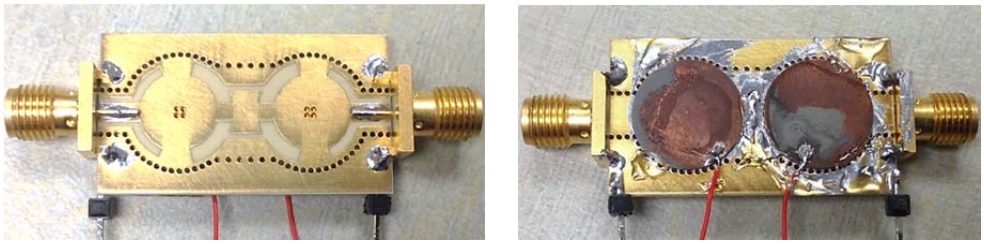

Figure 4.2 Fabricated evanescent mode cavity tuner, reprinted from [21]

Figure 4.3 shows the characterization of the evanescent mode cavity tuner. The characterization was obtained by varying the cavity position numbers and recording the corresponding reflection coefficients at all selected combinations of the position numbers. As seen in Figure 4.3, the tuner can present reflection coefficients covering most of the Smith Chart, which is very useful for reconfigurable circuitry. Furthermore, this coverage is provided with only two tuning elements. A lower quantity of tuning elements to control saves time in the overall reconfiguration process.

Figure 4.4 illustrates the stability of the tuner characterization. The figure depicts the resulting magnitude and phase of the tuner reflection coefficient, as well as the location of the reflection coefficient on the Smith Chart, for three different combinations of resonant cavity position numbers (n_1 and n_2) sent as inputs to the tuner. Each combination of n_1 and n_2 was input 1000 times in a row and the resulting value of reflection coefficient after each iteration was recorded. In other words, the tuner was

directed to the same setting 1000 times in a row for three different settings. As seen in Figure 4.4, there is drift in the characterization over time. Both the magnitude and phase of S_{11} drift in value between the first and the 1000th iteration for each of the three test combinations of n_1 and n_2. There are also occasional failures to tune to the correct setting, which are shown by the outliers on the plots. The Smith Chart plots for each test show the spread of the measured S_{11} points plotted as reflection coefficients. In the worst case, the magnitude of S_{11} varied by about 0.15 and the phase of S_{11} varied by 120° over the 1000 iterations even though the n_1 and n_2 setting was the same for each iteration. This has a significant impact on the ability to tune reliably. It was also found that physically moving the tuner changed the reflection coefficients of the characterized points. Tuning correctly and predictably to a point on the Smith Chart is a crucial step in reflection coefficient optimization algorithms. However, the characterization drift can be mitigated enough to be used for reflection coefficient optimization as long as the optimization is performed immediately after the characterization process finishes. This means that frequent recharacterization of the tuner is necessary.

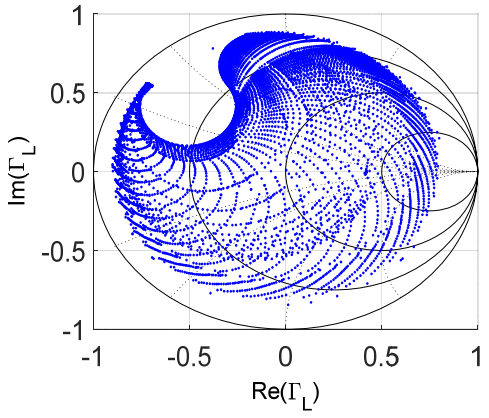

Figure 4.3 Characterization of the evanescent mode cavity tuner which maps cavity position numbers to reflection coefficients reachable by the matching network, reprinted from [35].

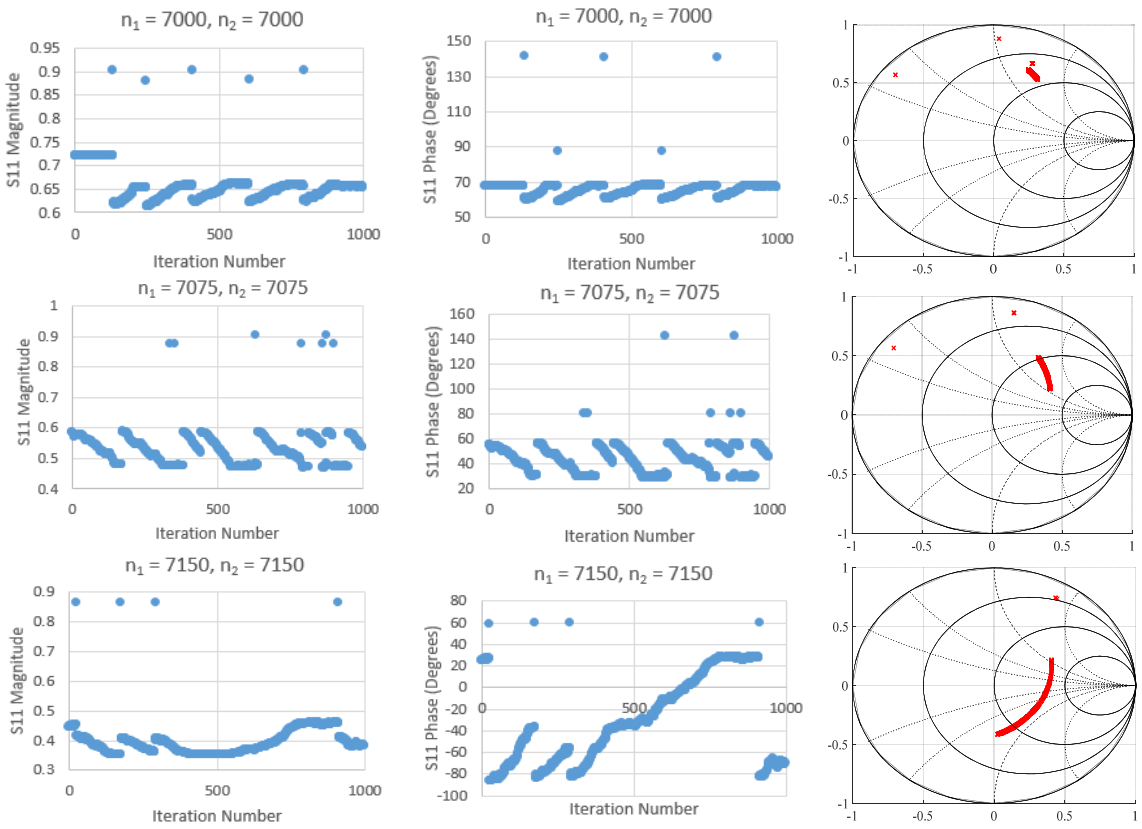

Figure 4.4 Measurement results showing characterization stability over time for three different (n_1, n_2) settings.

Reflection-Coefficient Tuning

Similar to the process described in Chapter Two, the power-amplifier PAE is optimized within an ACPR constraint by varying the load reflection coefficient presented by the evanescent mode cavity tuner using a gradient based optimization. A look-up table is used to determine the cavity position numbers to input to the tuner to obtain the characterized point that is closest to the load reflection coefficient needed. The optimization was tested using a MWT-173 FET, biased at $V_{GS} = -1.5$ V and $V_{DS} = 4.5$ V with 14 dBm input power. The ACPR constraint was -23 dBc. The input waveform was a modified chirp at 3.3 GHz. A chirp is a common signal used for radar. The

frequency of the signal increases over time. The modified chirp used for this experiment was mixed with a frequency at a single tone, which results in plenty of spectral spreading. The modified chirp signal is used to ensure that ACPR varies significantly with load reflection coefficient, which is convenient for verification of the spectrum compliance portion of the algorithm. To compare with the fast search algorithm, full load-pull measurements for PAE and ACPR were performed and are shown in Figure 4.5. The results of the load reflection coefficient optimization using the evanescent mode cavity tuner are shown in Table 4.1. Example search trajectories are shown in Figures 4.6 and 4.7.

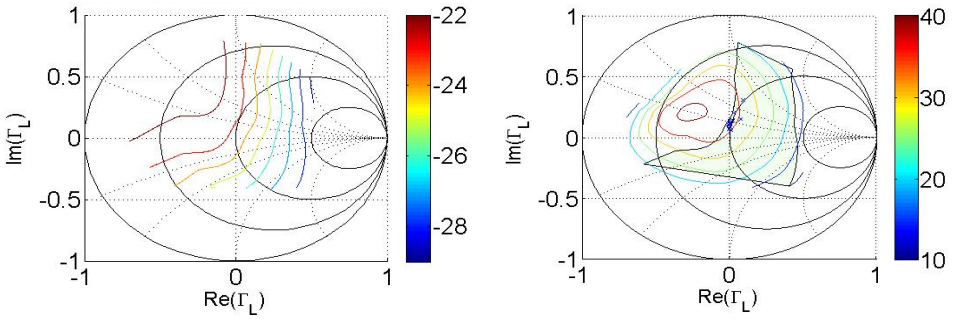

Figure 4.5 MWT-173 FET ACPR load-pull contours (left) and PAE load-pull contours with the ACPR acceptable region shaded and search endpoints marked with 'x' (right).

The data in Table 4.1 shows that, from several starting locations, the optimization converges to an ending location corresponding to the constrained optimum region identified in Figure 4.5. For each search, the ending location meets the ACPR constraint and obtains around 33.72% PAE in an average of 19.63 measurements. This verifies that the reflection coefficient optimization has been successfully implemented using the evanescent-mode cavity tuner as the tunable matching network with a characterized look-up table of reflection coefficients. Figures 4.6 and 4.7 demonstrate that the algorithm

determines a useful trajectory for arriving at an ending location in the region of the constrained optimum with few measurements. There is a fairly direct path from the starting location to the ending location in both figures, which is desired for an effective optimization.

Table 4.1 MWT-173 FET Optimization Results for Multiple Starting Locations Using Tunable Resonant Cavity Network as the Reconfigurable Matching Network

Start Γ_L	Start PAE (%)	End Γ_L	End ACPR (dBc)	End PAE (%)	# Meas.
0∠0°	32.95	0.11∠92.7°	-23.00	34.87	19
0.25∠0°	24.19	0.12∠88.0°	-23.07	34.06	16
0.25∠45°	29.54	0.13∠82.0°	-23.15	33.99	14
0.25∠90°	37.26	0.17∠62.2°	-23.29	33.51	17
0.25∠-45°	23.95	0.07∠90.9°	-23.26	33.47	27
0.25∠-90°	24.97	0.06∠77.6°	-23.18	33.85	21
0.25∠180°	30.63	0.11∠86.7°	-23.38	33.64	21
0.25∠-135°	28.71	0.32∠73.0°	-23.35	32.97	16
0.5∠0°	13.21	0.08∠86.3°	-23.26	33.21	13
0.5∠45°	21.51	0.13∠88.7°	-23.16	33.12	20
0.5∠90°	30.71	0.11∠88.6°	-23.15	34.14	29
0.5∠-135°	17.56	0.20∠82.8°	-23.49	33.37	30
0.5∠-90°	10.37	0.10∠94.2°	-23.25	33.44	18
0.7∠45°	10.59	0.14∠82.2°	-23.37	33.78	18
0.7∠90°	17.73	0.14∠79.7°	-23.1	33.98	18
0.7∠180°	5.73	0.07∠90.4°	-23.26	34.05	17
		Average	**-23.23**	**33.72**	**19.63**

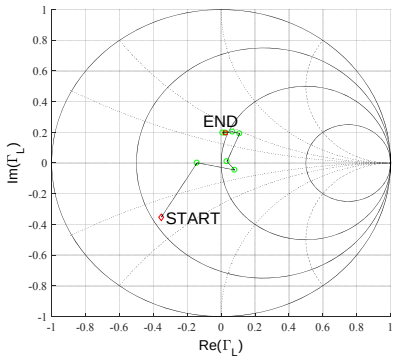

Figure 4.6 MWT-173 FET fast search from starting point $\Gamma_L = 0.5/\underline{-135°}$. The search converges to $\Gamma_L = 0.20/\underline{82.84°}$ with PAE = 33.37% and ACPR = -23.49 dBc using 30 measurements.

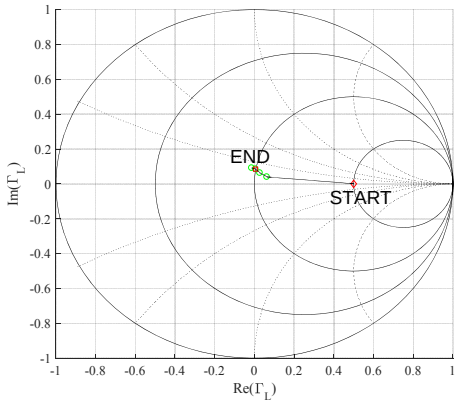

Figure 4.7 MWT-173 FET fast search from starting point $\Gamma_L = 0.5/\underline{0°}$. The search converges to $\Gamma_L = 0.08/\underline{86.31°}$ with PAE = 33.21% and ACPR = -23.26 dBc using 13 measurements.

The algorithm and the evanescent-mode cavity tuner were also tested on a Skyworks packaged amplifier. The second test was performed to illustrate that the algorithm and tuner are not device specific and can be used to optimize different devices. The amplifier supply voltage was 9 V and the input power was 6 dBm for these experiments. The ACPR constraint was -22 dBc. The input waveform was a modified chirp at 3.3 GHz. For comparison with the fast search results, Figure 4.4 shows the ACPR contours and PAE contours as measured from a full load-pull measurement. The results of the optimization are shown in Table 4.2. An example search trajectory is shown in Figure 4.9 and Figure 4.10.

Again, the data in Table 4.2 shows that, from several starting locations, the optimization converges to an ending location corresponding to the constrained optimum region identified in Figure 4.8. For each search, the ending location meets the ACPR constraint and obtains approximately 10.52% PAE in an average of 21.08 measurements. This verifies that the reflection coefficient optimization has been successfully implemented using the evanescent-mode cavity tuner as the tunable matching network

utilizing a characterized look-up table of reflection coefficients for more than one device. Figures 4.9 and 4.10 demonstrate that the algorithm determines a useful trajectory for arriving at an ending location in the region of the constrained optimum with few measurements.

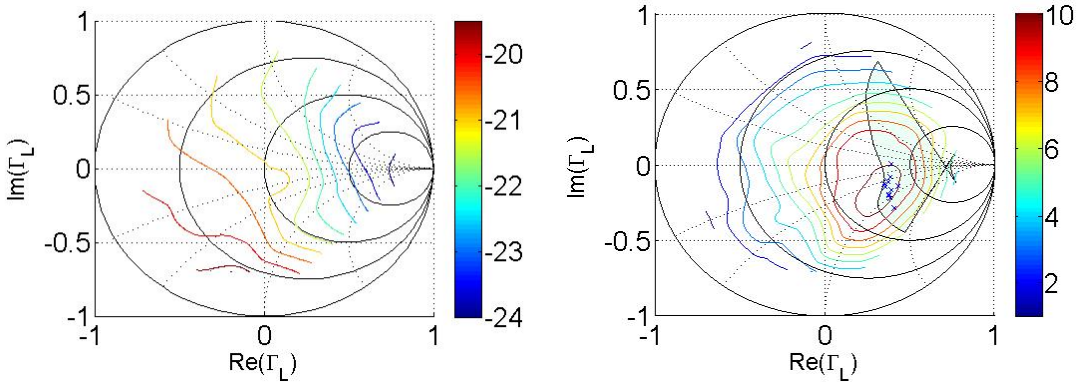

Figure 4.8 Skyworks amplifier ACPR load-pull contours (left) and PAE load-pull contours with the ACPR acceptable region shaded and search endpoints marked with 'x' (right).

Table 4.2 Skyworks Amplifier Optimization Results for Multiple Starting Locations Using Tunable Resonant Cavity Network as the Reconfigurable Matching Network

Start Γ_L	Start PAE (%)	End Γ_L	End ACPR (dBc)	End PAE (%)	# Meas.
0∠0°	8.23	0.43∠-28.24°	-22.05	10.69	23
0.25∠0°	10.22	0.39∠0.37°	-22.20	9.91	7
0.25∠45°	-0.43	0.43∠-23.68°	-22.02	10.61	24
0.25∠90°	7.34	0.44∠-29.91°	-22.08	10.60	17
0.25∠135°	6.01	0.42∠-27.58°	-22.17	10.67	26
0.25∠-135°	5.13	0.42∠-23.28°	-22.17	10.65	26
0.5∠0°	9.44	0.39∠-17.09°	-22.08	10.52	7
0.5∠45°	6.28	0.50∠-34.99°	-22.05	10.54	23
0.5∠90°	4.33	0.37∠-20.21°	-22.11	10.57	20
0.5∠-135°	4.05	0.45∠-18.19°	-22.38	10.54	30
0.5∠135°	3.65	0.39∠-12.13°	-22.07	10.17	22
0.5∠180°	2.28	0.38∠-28.24°	-22.01	10.74	28
		Average	**-22.11**	**10.52**	**21.08**

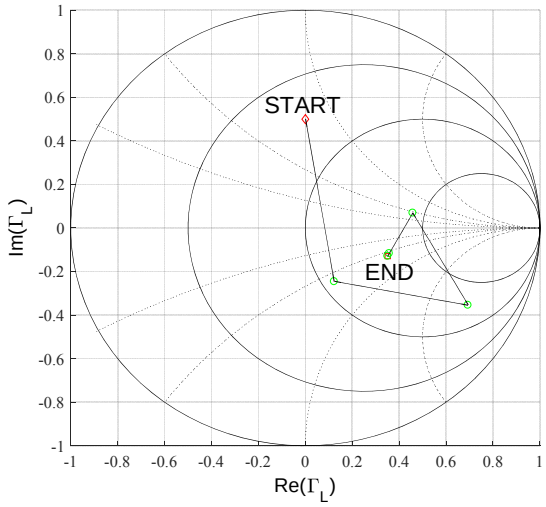

Figure 4.9 Skyworks packaged amplifier fast search from starting point $\Gamma_L = 0.5\underline{/90°}$. The search converges to $\Gamma_L = 0.37\underline{/\text{-}20.21°}$ with PAE = 10.57% and ACPR = -22.11 dBc using 20 measurements.

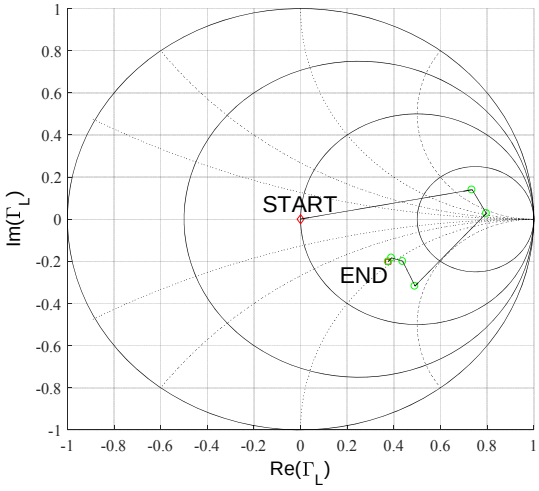

Figure 4.10 Skyworks packaged amplifier fast search from starting point $\Gamma_L = 0\underline{/0°}$. The search converges to $\Gamma_L = 0.43\underline{/\text{-}28.24°}$ with PAE = 10.69% and ACPR = -22.05 dBc using 23 measurements.

Note that the initial step in the optimization shown in Figure 4.10 is not in the expected direction based on the device contours. As stated previously, characterization drift and occasional failures to tune can negatively impact the optimization. In this case, the characterized location for one of the neighboring points of the first candidate drifted

during the time between the characterization and the measurement. As a result, the gradient estimation was thrown off and the first step was taken in the wrong direction. However, most of the other Γ_L locations used in the search were reliably characterized, so the optimization was able to recover after the initial step and converge at the expected final Γ_L location.

These optimizations were performed immediately after the tuner characterization was measured. If the optimization is performed several hours after the characterization has finished, the characterization is more subject to drift which throws the optimization off so that it does not converge to an acceptable end location. Figure 4.11 shows an example of a search that was performed 24 hours after the characterization and as a result, did not converge in the correct location. The device under test was a MWT-173 FET, biased at $V_{GS} = -1.5$ V and $V_{DS} = 4.5$ V with 14 dBm input power. The ACPR constraint was -23 dBc. Based on the contours shown in Figure 4.5, the search should have ended in a location similar to the ending locations obtained in Figures 4.6 and 4.7 and obtained a final PAE value of about 33%. Instead, the search ended near the right side of the Smith Chart and obtained a final PAE value of 16.01%. The first three steps are large steps made in very different directions, indicating that the gradient estimation is inaccurate due to characterization drift.

In conclusion, through the use of a look-up table, the reflection coefficient of the evanescent mode cavity tuner can be used to optimize performance of a transmitter power-amplifier. The main advantages of the tuner for use in next generation reconfigurable radar systems are its power handling and bandwidth. However, in its current state, the stability of the characterization is degraded over time and is sensitive to

physical movement. Therefore, the characterization must be re-measured frequently and the load reflection coefficient optimization must be performed immediately after the characterization process for accurate performance.

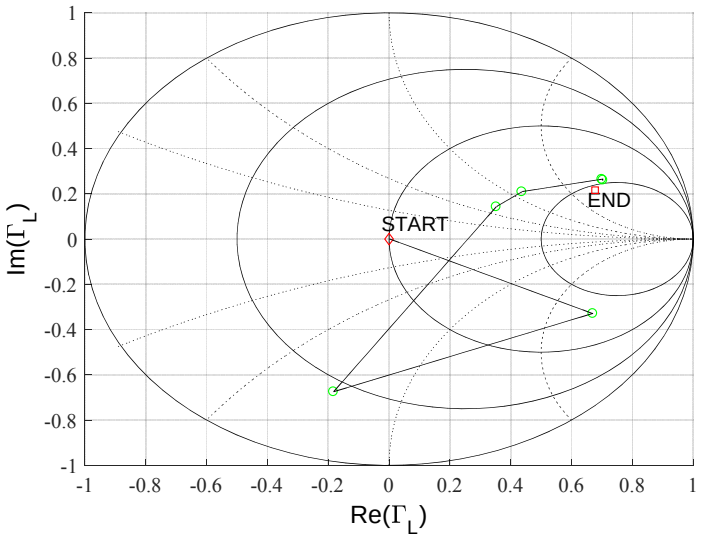

Figure 4.11 MWT-173 FET fast search performed 24 hours after tuner characterization from starting point $\Gamma_L = 0/\underline{0°}$. The search incorrectly converges to $\Gamma_L = 0.71/\underline{17.70°}$ with PAE = 16.01% and ACPR = -25.54 dBc using 19 measurements.

Simplex Tuning in Resonant Cavity Number Space

As research had been performed on the direct tuning of the control element of the tunable-varactor matching network, a similar study was performed directly tuning the cavity position numbers of the evanescent mode cavity tuner to optimize amplifier performance. Directly tuning the cavity position numbers allows for simpler implementation because the characterization process and look up table are no longer needed [36]. In addition, the optimization is not subject to the instability of the tuner characterization. The search space also remains two dimensional as there are only two cavities to control.

However, as shown in Figure 4.12, there are non-convexities of the contours in the cavity position number search space. The contours were measured for a Skyworks packaged amplifier with a control voltage of 7 V and an input power of 3 dBm. Rezayat demonstrates that the gradient based search only consistently converges to the optimum point if the search starts near the optimum [34].

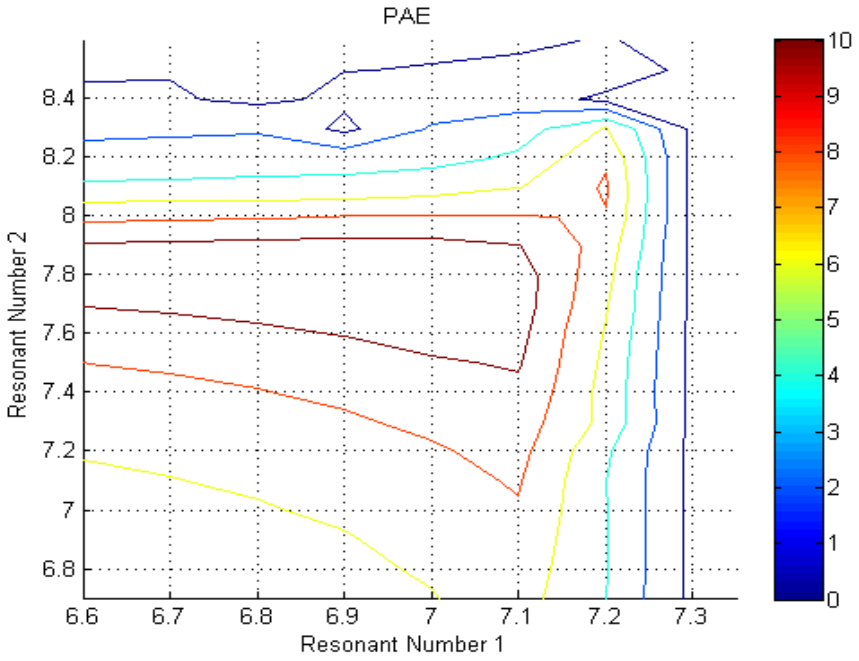

Figure 4.12 Skyworks packaged amplifier PAE contours in the cavity position number search space

Therefore, a simplex search was implemented to optimize the cavity position numbers to obtain maximum amplifier PAE. The simplex algorithm is described in Figure 4.13.

The first point of the simplex is shown in Figure 4.13 as point A. Additional points are measured in each coordinate direction separated by D_S, forming a right triangle. The point with the lowest PAE is replaced with a new point. If point A has the

lowest PAE, then point 1 is measured. If point 1 has a greater PAE than points A, B, and C, then point 2 is measured. If the PAE of point 2 is lower than point 1, then the new simplex consists of points B, C, and 1 and the process begins again. If the PAE of point 1 is greater than point A but less than points B and C then the new simplex contains points B, C, and 4. Finally, if point 1 has a lower PAE than point A, then the new simplex consists of points B, C, and 3. The search iterates through this process until the distance from the centroid to the new simplex points falls below a resolution distance (D_r) set by the user. The point with the highest PAE is chosen as the optimum.

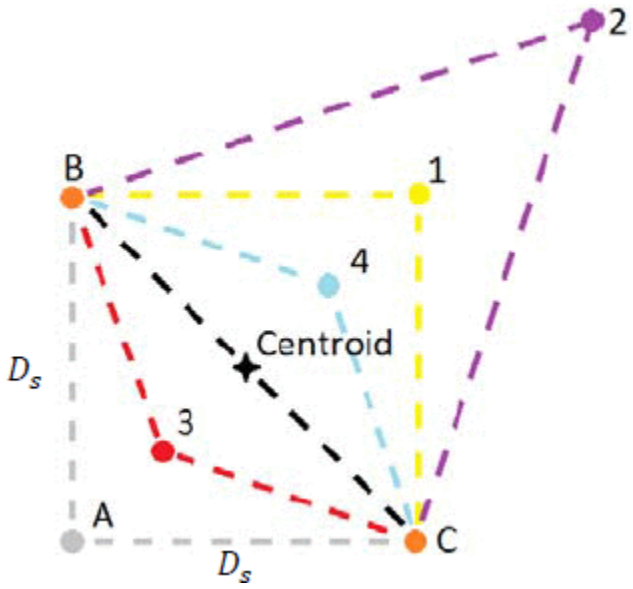

Figure 4.13 Simplex construction for PAE optimization in the cavity position number search space, reprinted from [36].

The summary of the results of the simplex search tested on the Skyworks amplifier are shown in Table 4.3. An example search trajectory is shown in Figure 4.14.

As seen in Table 4.3, the results show convergence to similar PAE values for multiple starting (n_1, n_2) combinations with a small number of measurements. The advantages of this type of search include simpler implementation by avoiding the need

for tuner characterization, and removing the need for prior knowledge about the device contours to choose an intelligent starting location. The simplex search converges even for starting locations far from the optimum, as shown in Figure 4.14.

Table 4.3 Skyworks Amplifier Simplex PAE Optimization Results for Multiple Starting Locations Using Tunable Resonant Cavity Network as the Reconfigurable Matching Network in the Resonant Cavity Position Number Search Space

Start n_1	**Start n_2**	**End n_1**	**End n_2**	**End PAE**	**Number of Meas.**
6690	8360	6985	7723	12.38	24
6400	8000	6988	7754	12.36	22
6400	7500	6988	7750	12.37	27
7000	7500	6983	7751	12.35	15
7000	7700	6987	7748	12.37	13
6200	8400	6965	7734	12.35	25
6700	7400	6980	7728	12.36	20
7000	8000	7000	7741	12.36	22
			Average	12.36	21.00

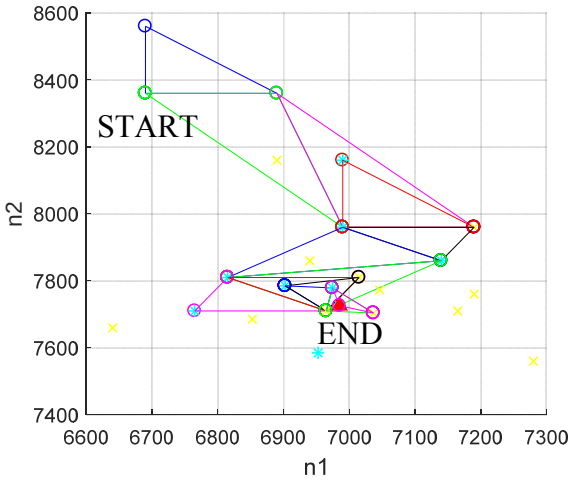

Figure 4.14 Fast simplex search starting at the point (6690, 8360). The search ended at the point (6985, 7723) with 12.38% PAE in 24 measurements.

In conclusion, the cavity position numbers of the evanescent mode cavity tuner can be tuned directly using a simplex algorithm to obtain maximum amplifier PAE. The

gradient search with intelligent starting location can also be used. The gradient search spends less time in regions that are not in ACPR compliance, and it is easier to select the starting step size and ending step size criteria using the gradient search [34]. The simplex search can converge from more starting locations but it is less intuitive to determine the necessary ending criteria. However, both methods of direct tuning of the resonant cavity position numbers remove the need for the lengthy characterization process and overcomes the problem of characterization instability.

CHAPTER FIVE

Stability Considerations

Power-amplifier stability is normally assessed for a single load reflection coefficient at the design frequency. However, in a reconfigurable amplifier, a method to assess stability in real time with varying load reflection coefficient and frequency is necessary. In some cases, the device may initially be operating stably, but then enter an unstable region during optimization.

Broadband Stability Design

Information in this section has been published as:
[37] L. Lamers, E. Walden, C. Baylis and E. V. R. J. Marks, "Fast Design of Unconditionally Stable Power-amplifier Using the Center Frequency Smith Tube," *2017 Texas Symposium on Wireless and Microwave Circuits and Systems (WMCS)*, Waco, TX, 2017, pp. 1-4

In amplifier design, a first step in the process is to use the device S-parameters to calculate and plot a stability circle on the Smith Chart. The load stability circle identifies regions of load reflection coefficients resulting in stable operation and potentially unstable operation. If the stability circle intersects the Smith Chart, the device is not unconditionally stable. If unconditional stability is desired, the designer can often add a stabilizing resistor either in feedback or in shunt or series configuration at the input or output. After the amplifier is designed, the stability factor K and the determinant of the S-parameter matrix Δ can be plotted over a range of frequencies to assess broadband device stability, where

$$K = \frac{(1 - |S_{11}|^2 - |S_{22}|^2 + |\Delta|^2)}{2|S_{12}S_{21}|}, \tag{12}$$

and

$$\Delta = S_{11}S_{22} - S_{12}S_{21}. \tag{13}$$

In many situations, though the device appears unconditionally stable at the design frequency according to the stability circles, K or Δ may identify potential instability at frequencies other than the design frequency. As described by Gonzalez, for an unconditionally stable circuit, $K > 1$ for all frequencies and $|\Delta| < 1$ [26].

A new design tool was innovated to allow for broadband stability design of power-amplifiers. A three-dimensional extension of the Smith Chart with various parameters plotted on the z-axis has been used for circuit optimization in the literature [20, 39, 40]. A similar three-dimensional extension of the Smith Chart with center frequency on the z-axis is used for small-signal stability analysis for design, shown in Figure 5.1. Rather than plotting a stability circle at a particular frequency, a stability surface is plotted over a range of frequencies. Thus the designer can visualize potentially unstable load reflection coefficients over the range and can quickly choose a resistor to stabilize the amplifier or select a load reflection coefficient that is stable over a specified bandwidth. Using this tool, if unconditional stability is required, the stability surface must lie completely outside of the frequency Smith Tube.

To demonstrate the use of the center frequency Smith Tube in an amplifier design application, an amplifier design was performed using the traditional Smith Chart method and the new Smith Tube method. The results of each design were compared. For this experiment, a small-signal amplifier design was performed in Keysight's Advanced Design Systems simulation software. The simulation used a built-in NPN BJT model

biased at $V_{CE} = 4.95\ V$ and $I_{BB} = 100\ \mu A$. In a bipolar junction transistor (BJT), the device is biased by injecting a base current (I_{BB}) which forward biases the base-emitter junction as seen in Figure 5.2. The design frequency for the simulation experiment was 1 GHz. Two designs were compared, one using the Smith Chart and the other using the center frequency Smith Tube for broadband stability analysis. The gain of the amplifier at the design frequency was about 16 dB for both designs. The stability circle for this device at the bias point is shown in Figure 5.2.

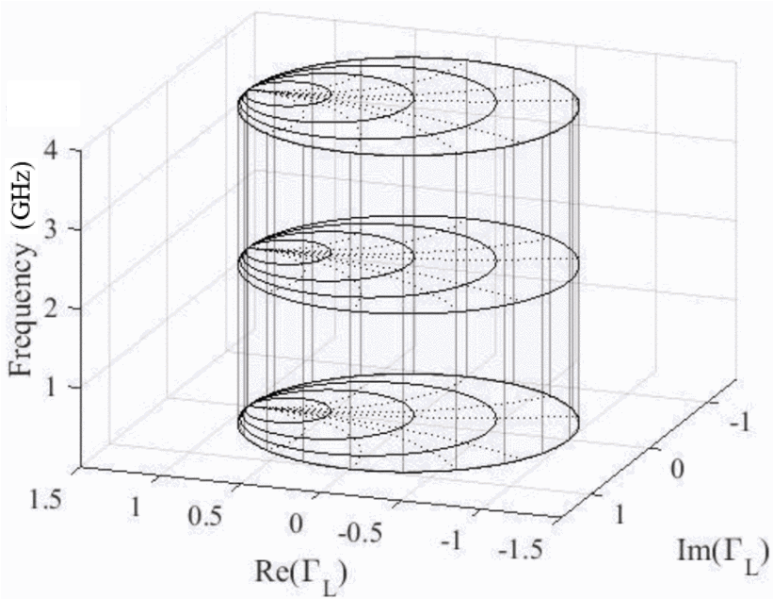

Figure 5.1 Center frequency Smith Tube used for broadband small-signal stability analysis

A typical amplifier design procedure using S-parameters is outlined by Gonzalez in [26]. After initial assessment of the small-signal stability circle at the design frequency, the designer may add a stabilizing resistor. The designer would then select a transistor bias setting and design a biasing network. Next the designer would identify the source and load reflection coefficients to obtain the desired amplifier gain and design a

matching network which presents those source and load reflection coefficients to the device. Once the amplifier schematic is designed, the designer can use the resulting circuit S-parameters to perform stability analysis by checking the values of K and Δ over a range of frequencies.

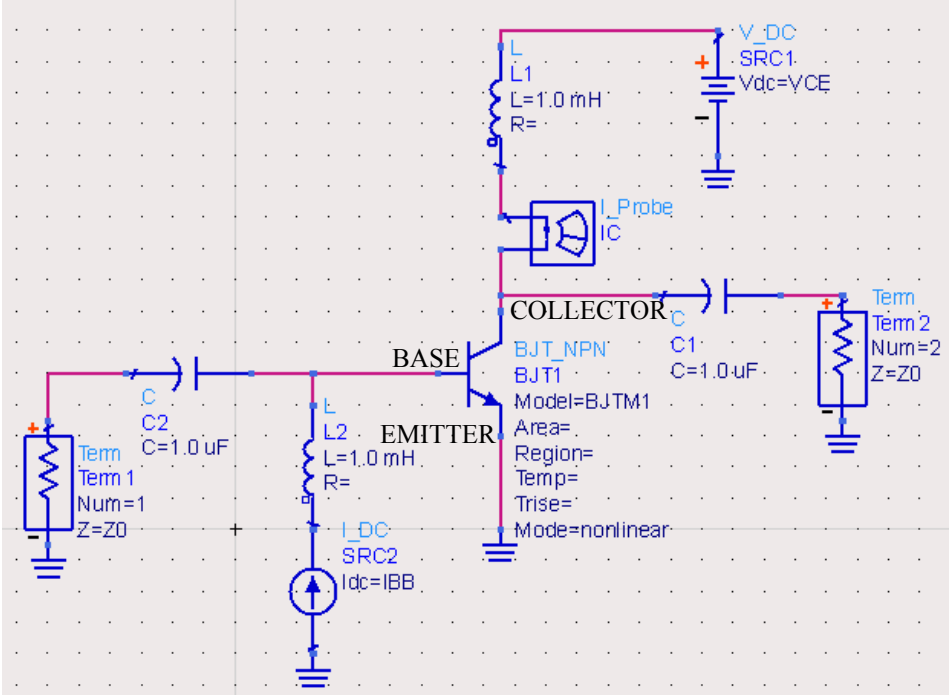

Figure 5.2 BJT circuit schematic showing how V_{CE} and I_{BB} are applied to bias the transistor

With the stability circle shown in Figure 5.3 and using the Smith Chart design procedure as outlined above, the designer may choose to add a 600 Ω stabilizing shunt resistor on the output to ensure that the stability circle lies well outside of the Smith Chart. The new stability circle with such a stabilizing resistor added is shown in Figure 5.4. Using only the Smith Chart at the design frequency, the designer may think the 600 Ω resistor is sufficient for providing unconditional stability.

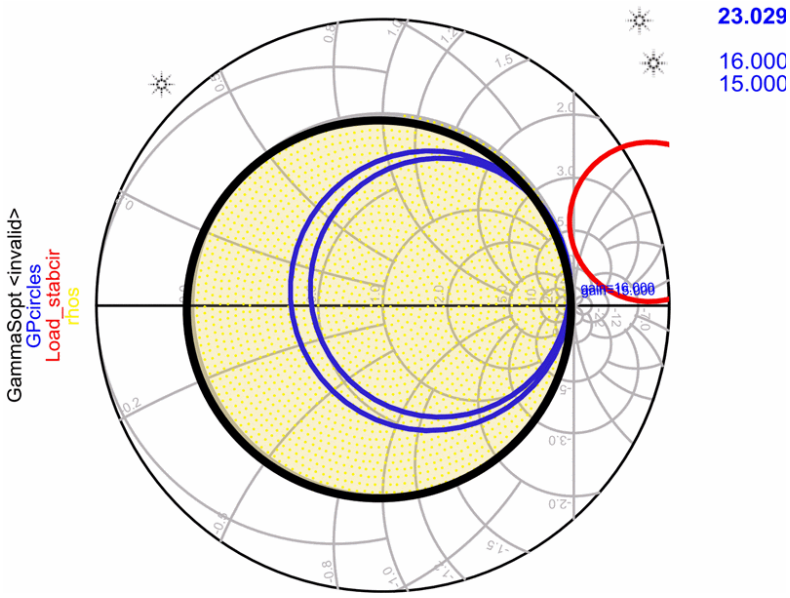

Figure 5.3 The simulated stability circle for the device under test. The stability circle lies outside of, but close to the edge of the Smith Chart. A stabilizing resistor may be added in the design to move the stability circle farther out and ensure that the device will be unconditionally stable.

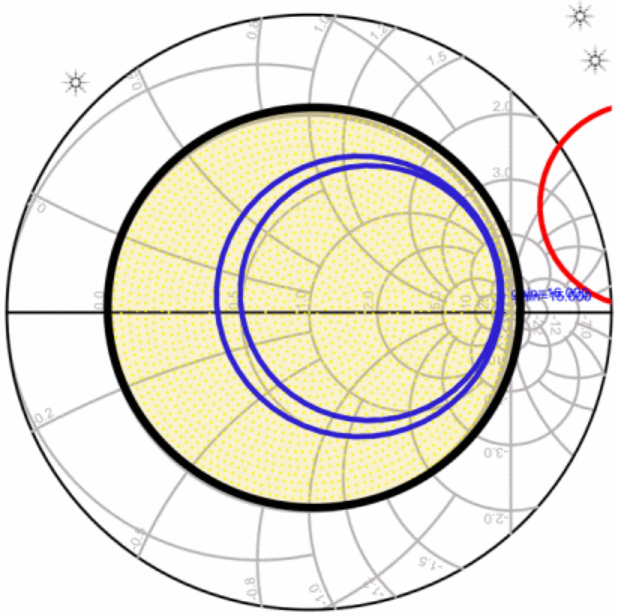

Figure 5.4 Simulated stability circle for the device under test with the 600 Ω stabilizing resistor. The stability circle is now well outside the Smith Chart

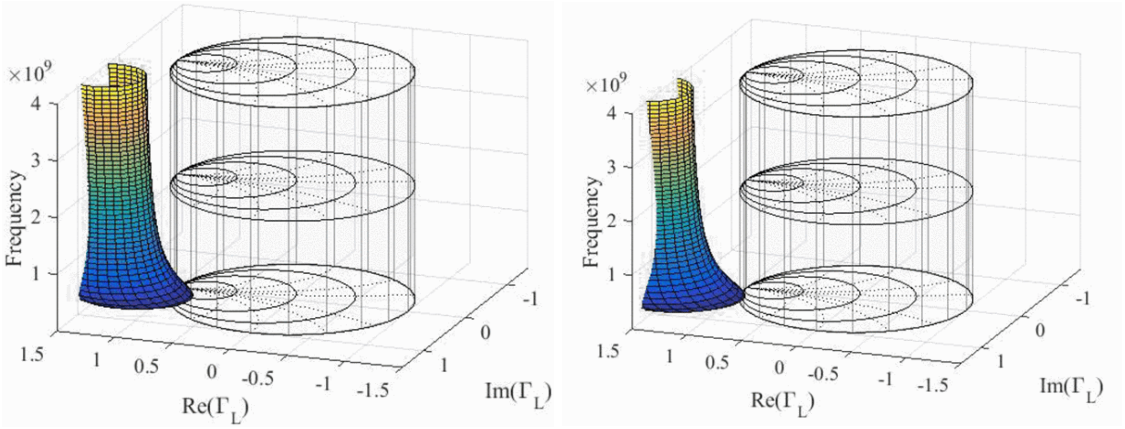

Figure 5.5 Stability surfaces plotted on the center frequency Smith Tube for the device (left) and the device with the 600 Ω stabilizing resistor added (right). Both surfaces intersect the Smith Tube, at low frequencies, showing that unconditional stability is not achieved.

In contrast, the stability surface plotted on the center frequency Smith Tube for the original device and the device with the 600 Ω resistor is shown in Figure 5.5. Using the broadband stability analysis tool, the designer can see that the 600 Ω resistor is not sufficient for achieving unconditional stability at all frequencies as the stability surface still intersects the Smith Tube at low frequencies. Therefore the designer could instead use a 300 Ω stabilizing shunt resistor at the output, resulting in the stability surface shown in Figure 5.6.

As seen in the figure, the 300 Ω resistor does provide unconditional stability. These results are verified by Figure 5.7, which compares the plot of the stability factor (K) for the design with the 600 Ω resistor to the design with the 300 Ω resistor. For unconditional stability, the stability factor must be greater than one for all frequencies, which is achieved by the second design but not the first.

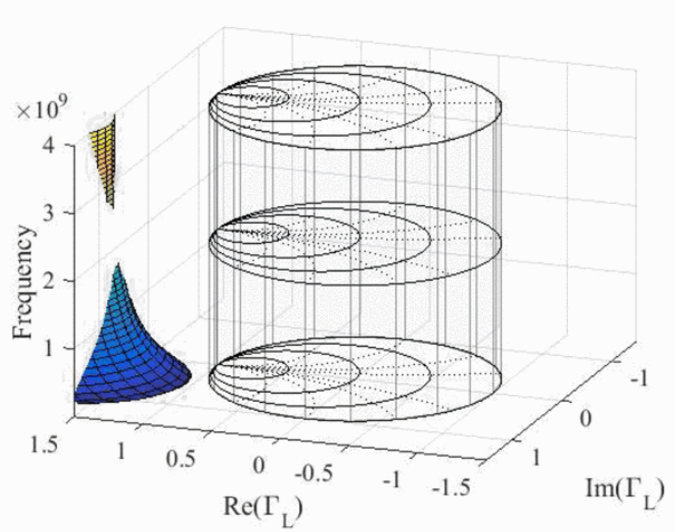

Figure 5.6 Simulated stability surface plotted for the device with the 300 Ω resistor added. The stability surface lies completely outside of the Smith Tube at all frequencies, showing that unconditional stability for small-signal inputs is achieved.

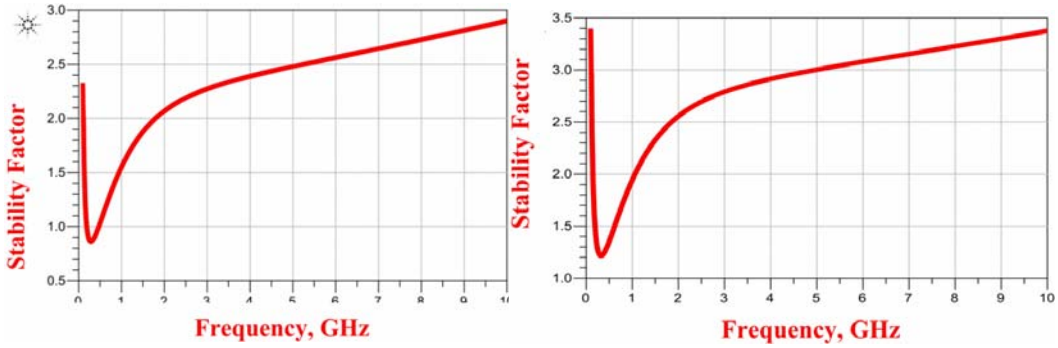

Figure 5.7 Stability factor (*K*) plots for the design obtained using only the Smith Chart (left) and using the Smith Tube (right). The stability factor falls below one using the conventional design method, showing that unconditional stability is not achieved. In contrast, the stability factor is greater than one for all frequencies when the broadband stability analysis method is used, showing that uncondtional stability is achieved.

The final design obtained using the center frequency Smith Tube for broadband stability analsysis is shown in Figure 5.8. Compared to the conventional method for amplifier design, the frequency Smith Tube method saves time and frustration. The frequency Smith Tube provides a way to visualize the amplifier's stability and other parameters over frequency. In conclusion, the frequency Smith Tube can be used to

visualize amplifier stability for small-signal inputs over a range of frequencies, which is useful for any design application in which broadband or reconfigurable performance is desired.

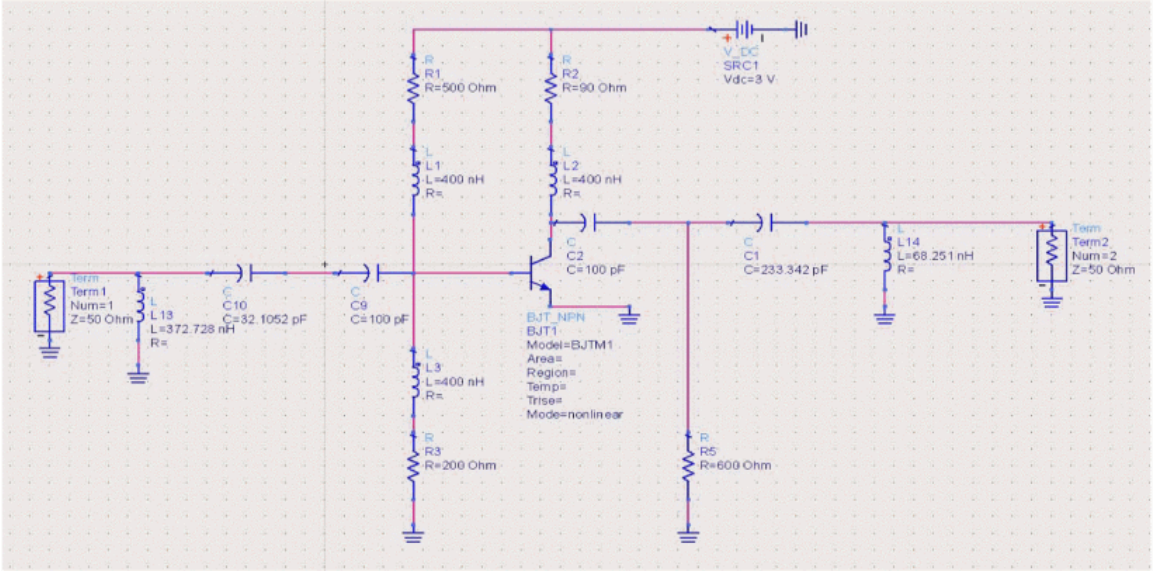

Figure 5.8 Final amplifier design obtained using the Smith Tube as a broadband design tool

Real Time Stability Analysis

Information in this section has been presented as [41] Hays, L.; Egbert, A.; Kappelmann, C.; Baylis, C.; Marks, R.; Viveiros, E.; "Real-time Transistor Stability Measurements Utilizing Acceleration of the Gain for the Next Generation Radar" USNC-URSI National Radio Science Meeting, January 2018, Boulder, Colorado

As the load reflection coefficient of the device changes during reconfiguration, a method of assessing the device stability in real time can help to protect the device and the system. A method was developed which uses the acceleration of the gain as an indicator of stability during power-amplifier operation. During a gain optimization of a device, the load reflection coefficient Γ_L will move towards the region of potential instability. As the load reflection coefficient gets closer to the unstable region, the rate of increase of the

gain is expected to grow larger, approaching infinity as the stability circle is approached. This indicates that the acceleration of the gain is positive. This can be seen in Figure 5.9. Point 1 on the Smith Chart is farthest away from the stability circle and has the lowest gain. As steps are taken closer to the stability circle, the gain increases with positive acceleration. Mathematically, since the stability circle corresponds to reflection coefficients which provide infinite gain, the acceleration of the gain must be positive when approaching the stability circle from a point with finite gain [26]. Thus, the acceleration of the gain can be measured and used as a metric to assess stability.

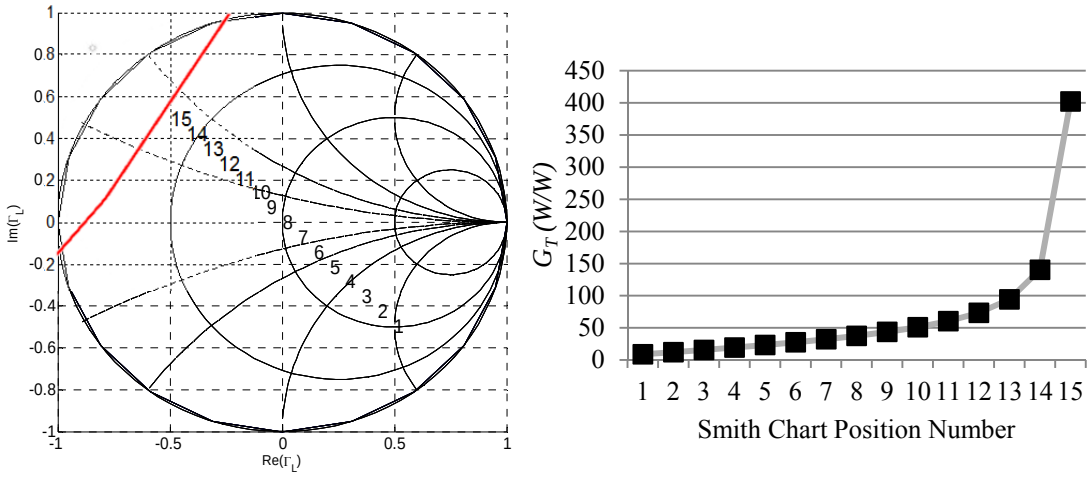

Figure 5.9 Transducer gain versus position on the Smith Chart for a device whose stability circle is shown (left). The position on the Smith Chart corresponds to the points shown.

Using the process outlined in Chapter Two, a gradient-based optimization of Γ_L can be performed to achieve maximum transducer gain from the device. During the optimization, stability analysis is performed in a real-time amplifier reconfiguration scenario. The acceleration of the gain is calculated and used to determine if the search should be stopped due to imminent oscillation. The algorithm presented in Chapter Two

is modified to include two additional neighboring point Γ_L measurements for each candidate Γ_L in the optimization for a total of four neighboring points as shown in in Figure 5.10. At each candidate and neighboring point, the gain in dB is measured. After each candidate point, two neighboring points (N_1 and N_2) are measured in the *x* and *y* directions. The gradient of the gain is estimated and the next two neighboring points (N_3 and N_4) are measured in the direction of increasing gain. These measurements are used to calculate the acceleration of the gain. Positive acceleration of the gain is used as an indicator that the device is potentially unstable, and that the search should be stopped before the unstable region of the Smith Chart is reached. Specifically the acceleration of the gain, A_G, is defined as:

$$A_G(C) = \frac{\{[G_T(N_4) - G_T(N_3)] - [G_T(N_3) - G_T(C)]\}}{D_n}, \tag{14}$$

where D_n is the neighboring-point distance. If two positive values of acceleration are obtained, the optimization is terminated at the candidate point with the current largest gain. If the acceleration does not indicate that the search is approaching instability, the optimization will end when the search step size is reduced to a specified limit, as outlined in Chapter Two.

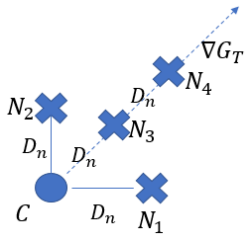

Figure 5.10 Points measured for each step of the load reflection coefficient optimization. Two small steps are taken along the x and y axis, and then two small steps are taken in the direction of the gradient of the gain. Each point is separated by a distance of D_n (0.05 for our experiments) on the Smith Chart.

A point of inflection in the acceleration of the gain is an indicator that the search may be nearing a region of instability. The search should be terminated at a stable Γ_L that results in a high gain. According to the theory, the acceleration of the gain will be positive and increasing as the search moves toward the unstable region. Based on this theory and on the results of several searches, many of which are shown below, stopping the search when A_G is positive for two consecutive candidates typically obtains the desired results when a starting search step size of 0.1 in the Smith Chart is used. The effectiveness of the stop criteria is related to the search step size, as a larger step size would direct the search into the unstable region in fewer measurements.

A modified search, with a directive to stop the gain when A_G is positive for two consecutive candidates, was performed for a Modelithics model of a Qorvo TGF 2960 pseudomorphic high electron mobility transistor (pHEMT). The simulation was performed under small-signal excitation at 3 GHz with bias $V_{DS} =$ 1.55 V, $V_{GS} =$ -0.2 V. The small-signal load stability circle, calculated from S-parameters, is shown in Figure 5.11. The stability circle lies completely outside of the Smith Chart so the device is unconditionally stable for all values of Γ_L under small-signal excitation. The optimization trajectory is shown in Figure 5.11, and Table 5.1 shows the data for all measured points. The optimization is never halted due to positive acceleration since the device is unconditionally stable. The final Γ_L provides a gain of 11.5 dB and the maximum available gain for the device calculated from the S-parameters is 12.6 dB. As expected for a stable device, the acceleration of the gain was consistently negative and the final gain obtained by the optimization was near and not over the maximum available gain for the device.

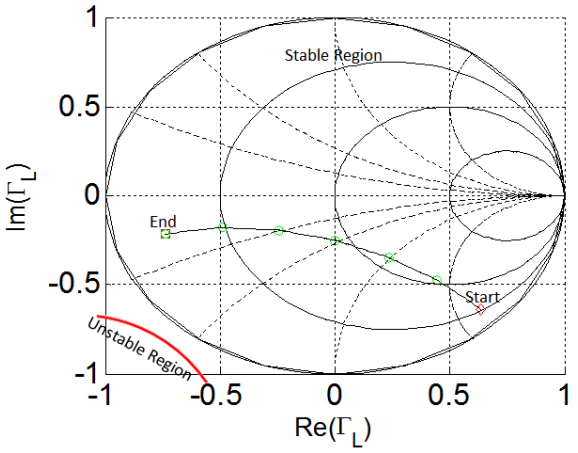

Figure 5.11 The stability circle and search trajectory for the Qorvo TGF 2960 Modelithics Model. The stability circle is completely outside the Smith Chart, so the device is unconditionally stable for small-signal inputs.

Table 5.1 Simulated Points for Gain Optimization of the Unconditionally Stable Qorvo TGF 2960 Modelithics Model with Acceleration Limit

	Γ_L	Gain (dB)	A_G
C_1	0.9∠-45°	0.947	-5.11
C_2	0.65∠-46.7°	6.375	-0.68
C_3	0.42∠-55.9°	8.695	-0.26
C_4	0.25∠-89.6°	10.162	-0.16
C_5	0.31∠-141.4°	11.172	-0.16
C_6	0.52∠-160.1°	11.769	-0.35
End	0.77∠-163.9°	11.523	-2.98

The same experiment was performed for several potentially unstable devices. If the gradient-based gain optimization following the method of Baylis [15], when no stability assessment is performed, a potentially unstable device may begin to oscillate. In harmonic balance simulations, the oscillatory behavior of the transistor generates unreasonable results such as large gain and negative input resistance values. Oscillatory behavior is seen in Table 5.2 by the negative input resistance value in the last row. The same Qorvo TGF 2960 PHEMT Modelithics behavioral model was used as the device under test; however, the simulation is performed under small-signal excitation at 2 GHz

and the device is biased differently with $V_{DS} = 5$ V and $V_{GS} = -1$ V. In this optimization scenario, the device is potentially unstable. The stability circle for this device is shown in Figure 5.12. If the search were stopped as soon as two consecutive positive acceleration values are determined, the search would have followed the trajectory shown in Figure 5.12 and would have been stopped after its sixth candidate (C_6) Γ_L (0.35∠134.1°), resulting in a gain of 18.21 dB. The maximum stable gain for this device is calculated as 19.96 dB. Using positive acceleration of the gain as a directive to terminate the search would maintain device stability while still obtaining a final gain value that is near, but not over the maximum stable gain.

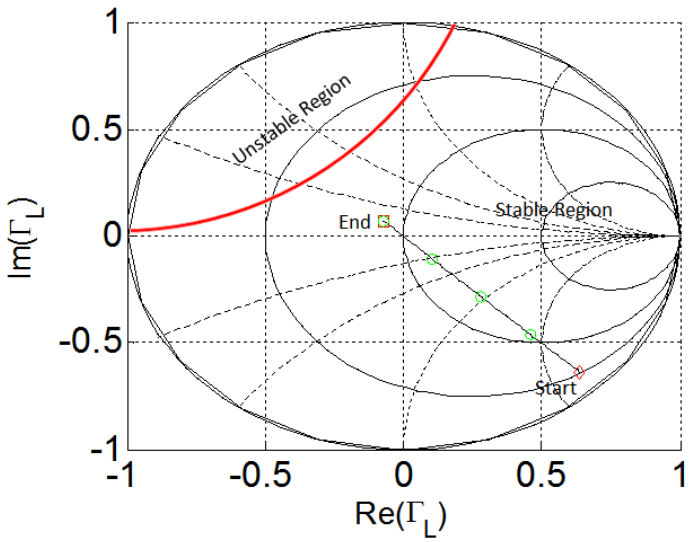

Figure 5.12 The stability circle and search trajectory for the Modelithics Qorvo TGF 2960 model. This search started at $\Gamma_L = 0.9\angle -45°$ and ended at $\Gamma_L = 0.4\angle 134.1°$ with a final gain of 18.2 dB.

Table 5.2 Simulated Points for Gain Optimization of the Potentially Unstable Qorvo TGF 2960 Modelithics Model with Acceleration Limit

	Γ_L	Gain (dB)	A_G	Real(Z_{in})
C_1	0.9∠-45º	4.53	-5.1	12.58
C_2	0.65∠-45.2º	10.23	-0.7	11.40
C_3	0.40∠-45.5º	12.87	-0.2	9.33
C_4	0.15∠-46.2º	14.76	-0.1	8.20
C_5	0.01∠135.4º	16.42	0.1	7.12
C_6	0.35∠134.1º	18.22	0.6	6.30
C_7	0.60∠133.1º	21.47	13.9	6.73
C_8	0.85∠129.8º	19.38	120.8	-142.88

To demonstrate that the acceleration limit successfully prevented oscillation for more than one device, the experiment was also performed in simulation for the built-in field effect transistor (FET) model provided in Keysight's Advanced Design System software and for a Modelithics model of an ON Semiconductor MMBFU310LT1 N-channel junction gate field-effect transistor (JFET). For each device, three different starting Γ_L locations were tested.

For the Keysight FET model the simulation was performed under small-signal excitation at 2 GHz with bias $V_{DS} =$ 5 V, $V_{GS} =$ -1 V. The stability circle and one of the search trajectories for this device are shown in Figure 5.13. A summary of the searches performed for this device is provided in Table 5.3. For all the starting locations, the search was terminated when two consecutive positive values of acceleration were obtained, which prevented the device from exhibiting oscillatory behavior in the simulator. All the searches ended near the same point and obtained similar final gain values.

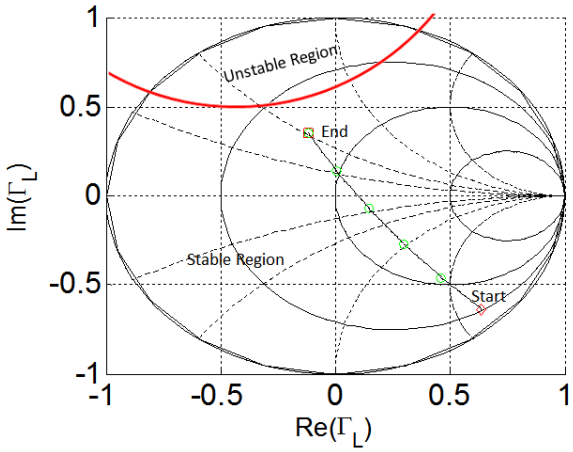

Figure 5.13 The stability circle and search trajectory for the Keysight FET model. This search started at $\Gamma_L = 0.9\angle -45°$ and ended at $\Gamma_L = 0.4\angle 108.7°$ with a final gain of 18.6 dB. The device never entered the unstable region or exhibited oscillation.

Table 5.3 Summary of Several Gain Optimizations of the Potentially Unstable Keysight FET Model with Acceleration Limit

Start Γ_L	End Γ_L	Final Gain (dB)
0.9∠-45°	0.4∠108.7°	18.6
0∠0°	0.3∠115.9°	17.3
0.3∠-60°	0.2∠113.9 °	16.9

For the Modelithics MMBFU310LT1 JFET model the simulation was performed under small-signal excitation at 0.5 GHz with bias $V_{DS} =$ 5.75 V, $V_{GS} =$ -0.8 V. The stability circle and one of the search trajectories for this device are shown in Figure 5.14. A summary of the searches performed for this device is provided in Table 5.4. For all the starting locations, the search was terminated when two consecutive positive values of acceleration were obtained, which prevented the device from exhibiting oscillatory behavior in the simulator. All the searches ended near the same point and obtained similar final gain values.

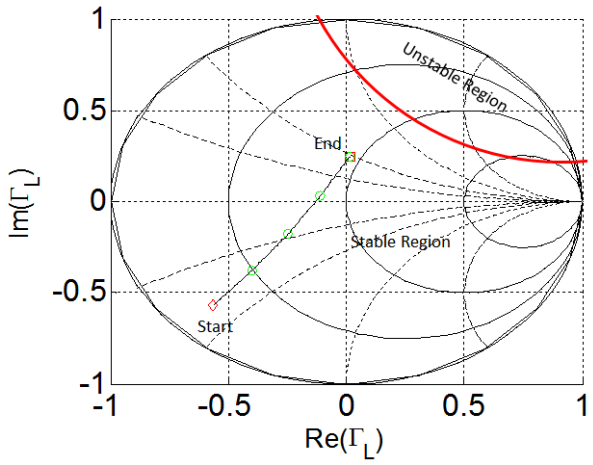

Figure 5.14 The stability circle and search trajectory for the Modelithics MMBFU310LT1 JFET model. This search started at $\Gamma_L = 0.8\angle -135°$ and ended at $\Gamma_L = 0.2\angle 87.1°$ with a final gain of 4.8 dB. The device never entered the unstable region or exhibited oscillation.

Table 5.4 Summary of Several Gain Optimizations of the Potentially Unstable Modelithics MMBFU310LT1 JFET Model with Acceleration Limit

Start Γ_L	End Γ_L	Final Gain (dB)
0.8∠-135°	0.2∠87.1°	4.8
0.3∠180°	0.4∠86.1°	6.0
0∠0°	0.3∠71.4 °	5.0

Finally, the search algorithm was measurement-demonstrated for a Microwave Technologies GaAs FET (MWT-173). For small-signal inputs at 4.44 GHz and for bias voltage combination V_{GS} = -1.5 V, V_{DS} = 4.5 V the device is unconditionally stable. Figure 5.15 and Table 5.5 show the data for all measured points. In measurement, due to noise, some points may have positive acceleration even though the device is not nearing instability. However, waiting for two consecutive positive acceleration values before terminating the search prevented the search from ending prematurely. For the stable device and a search step size of 0.1, consecutive positive acceleration values were never

obtained. Oscillation was never observed on the spectrum analyzer output during the search, as is expected for an unconditionally stable device.

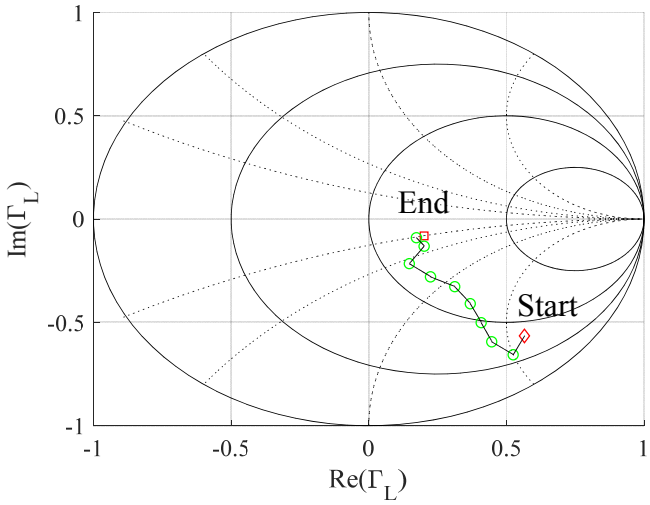

Figure 5.15 The search trajectory for the MWT-173 GaAs FET. This search started at $\Gamma_L = 0.84\angle -51.4°$ and ended at $\Gamma_L = 0.24\angle -33.17°$ with a final gain of 8.73 dB. The device never exhibited oscillation.

Table 5.5 Measured Points for Gain Optimization of Unconditionally Stable MWT-173 Under Small-Signal Excitation

	Γ_L	Gain (dB)	A_G
C_1	0.84∠-51.4°	4.23	5.4
C_2	0.74∠-53.1°	5.68	-2.8
C_3	0.65∠-50.9°	6.85	0.3
C_4	0.55∠-48.0°	7.63	-0.4
C_5	0.45∠-46.3°	8.22	3.1
C_6	0.36∠-51.3°	8.42	-1.6
C_7	0.26∠-55.7°	8.58	1.2
End	0.24∠-33.2°	8.73	-2.1

The search algorithm was also measurement-demonstrated for a different Microwave Technologies GaAs FET (MWT-173). For small-signal inputs at 4.44 GHz and for bias voltage combination $V_{GS} =$ -1.5 V, $V_{DS} = 5$ V the device is potentially unstable. Figure 5.16 and Table 5.6 show the data for all measured points. The search

was allowed to continue until the device became unstable to demonstrate that the device begins to oscillate soon after two consecutive positive values of acceleration are obtained. Oscillation was determined by observation of the spectrum analyzer output for the device, which is shown in Figure 5.17. If the acceleration limit was used, the search would have stopped after the second consecutive positive acceleration value – at the eighth candidate point with a gain of 17.8 dB and would not have oscillated.

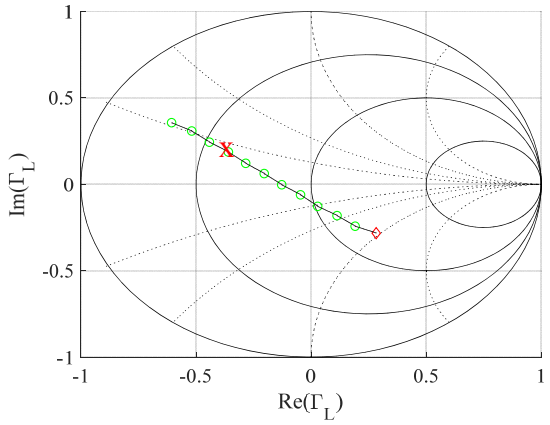

Figure 5.16 The search trajectory for the unstable MWT-173 GaAs FET. This search started at $\Gamma_L = 0.4\angle -45°$. With the acceleration limit, the search would have ended at $\Gamma_L = 0.41\angle 151.1°$ (marked by 'x') with a final gain of 18.65 dB.

Table 5.6 Measured Points for Gain Optimization of Potentially Unstable MWT-173 Under Small-Signal Excitation

	Γ_L	Gain (dB)	A_G
C_1	0.40∠-45°	12.37	0.0
C_2	0.31∠-51.8°	13.13	-0.5
C_3	0.21∠-58.1°	14.00	1.3
C_4	0.13∠-77.5°	14.73	-0.1
C_5	0.08∠-127.2°	15.51	0.1
C_6	0.13∠-178.8°	16.26	-0.5
C_7	0.21∠163.1°	17.05	0.2
C_8	0.31∠156.8°	17.82	0.01
C_9	0.41∠152.5°	18.65	0.3
C_{10}	0.50∠151.1°	19.57	0.9
C_{11}	0.60∠149.3°	20.66	162.2

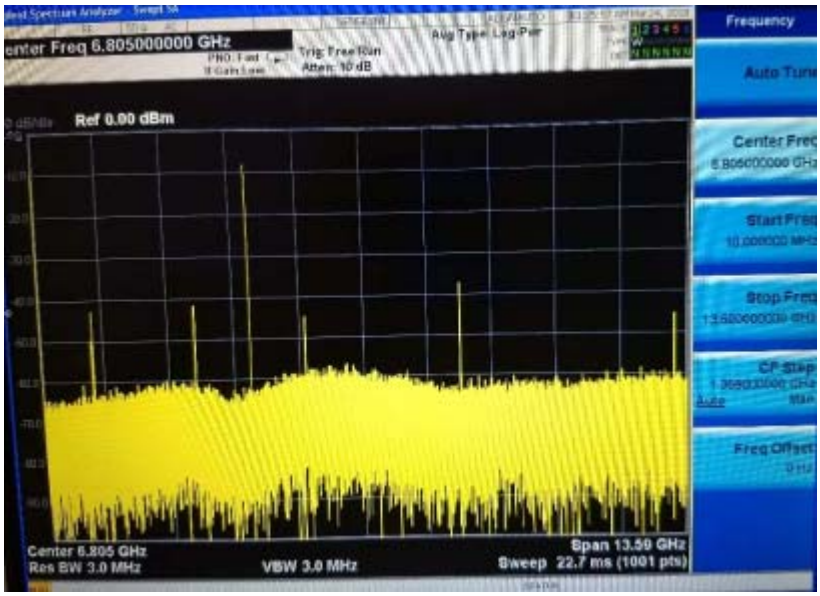

Figure 5.17 Spectrum analyzer output showing oscillation. The signal spikes at frequencies other than the center frequency and its harmonics are due to oscillation.

In conclusion, a method of analyzing stability during a real-time load reflection coefficient gain optimization has been presented and demonstrated in simulation and measurement under small-signal excitation. Though more measurement data would be useful, it has been shown for several devices that using the point of inflection in the acceleration of the gain as a limit, the gain maximization of a potentially unstable device is stopped before the device begins to oscillate. This method assumes that the optimization begins outside of the unstable region for the device. This method will be useful for maintaining stability for real-time reconfigurable circuitry as well as in standard device load-pull measurements in which an unstable device-under-test is a possibility.

CHAPTER SIX

Conclusions

This thesis has presented several methods for optimizing power-amplifiers which are implemented using state-of-the-art tunable matching networks for reconfiguration. A new broadband stability design visualization tool and a new stability analysis method for use during circuit reconfiguration have also been proposed. There are several key contributions of this thesis. Gradient based optimization that directly uses the fundamental tuning elements of the tunable matching network has been explored and compared to reflection coefficient tuning. A simplex method of optimization which directly uses the fundamental tuning elements of the tunable matching network has been shown to be useful in cases where the contours are not friendly to gradient optimization. A broadband stability design tool, which also has applications for reconfigurable circuitry, has been shown to identify regions of potential instability across a range of frequencies. Finally, the acceleration of the gain of an amplifier has been shown to be a useful metric for assessing device stability in real-time which does not require prior heavy computation or device characterization.

In future work, it is expected that these methods will be expanded and improved. The optimization methods for direct control of the fundamental tuning elements which were implemented on the tunable-varactor matching network and the evanescent mode cavity tuner can be applied to future tunable matching networks. The acceleration of the gain as a metric for stability assessment needs to be further explored in measurement and

for more devices. In some cases, the device under test may have positive acceleration of the gain for a short time, but still be operating stably. Exploring the characteristics of more devices will provide further insight on when to stop reconfiguration. It may be shown that an acceleration limit or allowing a device to reach a few more positive consecutive acceleration values will allow for higher gain while maintaining stable operation.

The big picture of the contributions of this thesis is that several challenges in reconfigurable circuitry for next generation radar systems have been explored. The methods presented will be useful for ensuring that the power-amplifier of the radar transmitter can operate efficiently and stably while maintaining spectrum compliance and can adaptively choose new operating parameters if the situation calls for reconfiguration. These methods can also be applied to other circuit reconfiguration problems for wireless applications other than radar.

BIBLIOGRAPHY

[1] Federal Communications Commission. Connecting America: The National Broadband Plan [Internet]. 2010 Mar. Available from: http://www.broadband.gov/plan/

[2] L.E. Brennan, I.S. Reed, "Theory of Adaptive Radar," IEEE Transactions on Aerospace and Electronic Systems, Vol. 9, No. 2, March 1973, pp. 237-252.

[3] S. Haykin, "Cognitive Radar: A Way of the Future," IEEE Signal Processing Magazine, January 2006, pp. 30-40.

[4] J. Guerci, "Cognitive Radar: The Knowledge-Aided Fully Adaptive Approach", Artech House, 2010

[5] J.S. Goldstein and I.S. Reed, "Theory of Partially Adaptive Radar," IEEE Transactions on Aerospace and Electronic Systems, Vol. 33, No. 4, October 1997, pp. 1309-1325.

[6] D. Qiao, R. Molfino, S. M. Lardizabal, "An Intelligently Controlled RF Power-amplifier With a Reconfigurable MEMS-Varactor Tuner," *IEEE Trans.on Microwave Theory and Tech.*, Vol. 53, No. 3, Part 2, March 2005, pp. 1089-1095.

[7] A. Martone, C. Dietlein, M. Govoni, K. Sherbondy and J. Pulskamp, "Tuning Technology for Adaptable Radar Bandwidth," 2016 IEEE MTT-S International Microwave Symp. (IMS), San Francisco, CA, May 2016.

[8] N. Kingsley and J.R. Guerci, "Adaptive Amplifier Module Technique to Support Cognitive RF Architectures," Proceedings of the 2014 IEEE Radar Conference, Cincinnati, Ohio, May 2014, pp. 1329-1332.

[9] J.-S. Fu and A. Mortazawi, "Improving Power-amplifier Efficiency and Linearity Using a Dynamically Controlled Tunable Matching Network," IEEE Transactions on Microwave Theory and Tech, Vol. 56, No. 12, December 2008, pp. 3239-3244.

[10] C. Baylis, M. Fellows, J. Barkate, A. Tsatsoulas, S. Rezayat, L. Lamers, R.J. Marks II, and L. Cohen, "Circuit Optimization Algorithms for Real-Time Spectrum Sharing Between Radar and Communications," 2016 IEEE Radar Conf. (RadarConf), Philadelphia, PA, May 2016.

[11] F. Yazdani and R. R. Mansour, "Realizing reconfigurable stub impedance matching networks using MEMS switches," *2017 47th European Microwave Conference (EuMC)*, Nuremberg, 2017, pp. 1081-1184.

[12] J. R. Perez-Cisneros *et al*., "2-D Optimization Methodology for Reconfigurable Transmitters by Tunable Matching Networks," in *IEEE Transactions on Circuits and Systems II: Express Briefs*, vol. 64, no. 11, pp. 1277-1281, Nov. 2017.

[13] H. S. Chen, Y. K. Hsieh and L. H. Lu, "A 5.5-GHz multi-mode power-amplifier with reconfigurable output matching network," *2015 IEEE Radio Frequency Integrated Circuits Symposium (RFIC)*, Phoenix, AZ, 2015, pp. 203-206.

[14] Z. Hays, C. Kappelmann, S. Rezayat, M. Fellows, L. Lamers, M. Flachsbart, J. Barlow, C. Baylis, E. Viveiros, A. Darwish, A. Hedden, J. Penn, and R.J. Marks II, "Real-Time Amplifier Optimization Algorithm for Adaptive Radio using a Tunable-Varactor Matching Network," *2017 IEEE Radio and Wireless Symposium (RWS)*, Phoenix, Arizona, January 2017, pp. 215-217.

[15] Lamers, L.; Hays, Z.; Baylis, C.; Marks, R.; Viveiros, E.; Penn, J.; Hedden, A.; Darwish, A, "Syndicated Test Bench Set-up for Testing of Real-time Reconfigurable Power-amplifiers for the Next Generation Radar." USNC-URSI National Radio Science Meeting, January 2017, Boulder, Colorado.

[16] M. Fellows, C. Baylis, J. Martin, L. Cohen and R. J. Marks, "Direct algorithm for the Pareto load-pull optimisation of power-added efficiency and adjacent-channel power ratio," in *IET Radar, Sonar & Navigation*, vol. 8, no. 9, pp. 1280-1287, 12 2014.

[17] M. Fellows, L. Lamers, C. Baylis, L. Cohen and R. J. Marks, "A Fast Load-Pull Optimization for Power-Added Efficiency under Output Power and ACPR Constraints," *IEEE Transactions on Aerospace and Electronic Systems*, Vol. 52, No. 6, December 2016, pp. 2906-2916.

[18] J. Barkate, A. Tsatsoulas, C. Baylis, L. Cohen and R. J. Marks, "Comparison of Multidimensional Circuit Optimization Techniques for Real-Time Transmitter Use," *2016 Texas Symposium on Wireless and Microwave Circuits and Systems*, Waco, Texas, April 2016.

[19] C. Baylis, M. Fellows, J. Barkate, A. Tsatsoulas, S. Rezayat, L. Lamers, R.J. Marks II, and L. Cohen, "Circuit Optimization Algorithms for Real-Time Spectrum Sharing Between Radar and Communications," *2016 IEEE Radar Conference (RadarConf)*, Philadelphia, PA, May 2016.

[20] J. Barkate, M. Flachsbart, Z. Hays, M. Fellows, J. Barlow, C. Baylis, L. Cohen, and R.J. Marks II, "Fast, Simultaneous Optimization of Power-amplifier Input Power and Load Impedance for Power-Added Efficiency and Adjacent-Channel Power Ratio using the Power Smith Tube," *IEEE Transactions on Aerospace and Electronic Systems*, Vol. 52, No. 2, April 2016, pp. 928-937.

[21] A. Semnani, M. Abu Khater, Y.-C. Wu, and D. Peroulis, "An Electronically-Tunable High-Power Impedance Tuner with Integrated Closed-Loop Control," *IEEE Microwave and Wireless Components Letters*, Vol. 27, No. 8, August 2017, pp. 754-756.

[22] A. Semnani and D. Peroulis, "Nano-Plasma Tunable Evanescent-Mode Cavity Resonators," 2014 IEEE MTT-S International Microwave Symposium (IMS). Tampa, Florida, June 2014.

[23] X. Liu, L. P. B. Katehi, W. J. Chappell and D. Peroulis, "High-Q Tunable Microwave Cavity Resonators and Filters Using SOI-Based RF MEMS Tuners," *Journal of Microelectromechanical Systems*, vol. 19, no. 4, Aug. 2010, pp. 774-784.

[24] M. Abu Khater, Y. C. Wu and D. Peroulis, "Tunable Cavity-Based Diplexer With Spectrum-Aware Automatic Tuning," *IEEE Transactions on Microwave Theory and Techniques*, Vol. 65, No. 3, pp. 934-944, March 2017.

[25] M. Abu Khater and D. Peroulis, "Real-Time Feedback Control System for Tuning Evanescent-Mode Cavity Filters," *IEEE Transactions on Microwave Theory and Techniques*, Vol. 64, No. 9, September 2016, pp. 2804-2813.

[26] G. Gonzalez, Microwave Transistor Amplifiers: Analysis and Design, Second Edition, Prentice-Hall, 1997.

[27] E. Carli, T. Corzani, "General Representation for the Rollet Stability Factor of a Two-Port Network," IEEE Transactions on Circuit Theory, 1969, v. 16, #2.

[28] A. Suarez, S. Jeon, D. Rutledge, "Global Stability Analysis and Stabilization of Power-amplifiers," 2008 Microwaves, Radar and Remote Sensing Symposium (2008 MRRS), September 2008.

[29] A. Subramaniam, M. Fadzil Ain, "Unified Approach for Large-signal stability analysis of 4 Watt UHF RF power-amplifier," 2011 IEEE 3rd International Conference on Communication Software and Networks (2011 ICCSN), May 2011.

[30] F.L. Traversa, F. Bonani, "Application of Floquet theory to the large-signal analysis of microwave amplifiers," 2013 IEEE 14th Annual Wireless and Microwave Technology Conference (2013 Wamicon), April 2013.

[31] A. Collado, A. Suarez, J.M. Collantes, "Large-Signal Stability Analysis of Microwave Amplifiers under Complex Modulated Signals with Time-Varying Envelope", *IEEE MTT-S International Microwave Symp.*, pp. 809-813, 2005, Jun., 2005.

[32] F. Di Paolo, G. Leuzzi, "Bifurcation Synthesis by Means of Harmonic Balance and Conversion Matrix", Proc. GAAS 2003, Munich, Germany, 2003, pp. 521-524.

[33] L. Lamers, Z. Hays, C. Kappelmann, S. Rezayat, M. Fellows, E. Walden, A. Egbert, C. Baylis, R.J. Marks II, E. Viveiros, J. Penn, A. Hedden, and A. Darwish, "Comparison of Bias-Voltage and Reflection-Coefficient Based Reconfiguration of a Tunable-Varactor Matching Network for Adaptive Amplifiers," *2017 IEEE 18th Wireless and Microwave Technology Conference (WAMICON)*, Cocoa Beach, FL, 2017.

[34] Hays, L.; Rezayat, S.; Baylis, C.; Marks II, R.; Viveiros, E.; Peroulis, D.; Abu-Khater, M.; Semnani, A.; “Direct Tuning of Cavity Position Numbers for Circuit Optimization Using an Evanescent-Mode Cavity Tuner Designed for Reconfigurable Radar Transmitters” USNC-URSI National Radio Science Meeting, January 2018, Boulder, Colorado

[35] Z. Hays *et al*., "Fast Impedance Matching Using Interval Halving of Resonator Position Numbers for a High-Power Evanescent-Mode Cavity Tuner," *2018 IEEE Radio and Wireless Symposium (RWS)*, Anaheim, CA, USA, 2018

[36] A. Tsatsoulas, J. Barkate, C. Baylis and R. J. Marks, "A simplex optimization technique for real-time, reconfigurable transmitter power amplifiers," *2016 IEEE MTT-S International Microwave Symposium (IMS)*, San Francisco, CA, 2016

[37] L. Lamers, E. Walden, C. Baylis and E. V. R. J. Marks, "Fast design of unconditionally stable power-amplifier using the center frequency Smith Tube," *2017 Texas Symposium on Wireless and Microwave Circuits and Systems (WMCS)*, Waco, TX, 2017, pp. 1-4.

[38] M. Fellows, M. Flachsbart, J. Barlow, C. Baylis and R. J. Marks, "The Smith Tube: Selection of Radar Chirp Waveform Bandwidth and Power-amplifier Load Impedance using Multiple-Bandwidth Load-Pull Measurements," 2014 IEEE Wireless and Microwave Technology Conference (WAMICON 2014), Tampa, Florida, June 2014.

[39] J. Barkate, A. Tsatsoulas, M. Fellows, M. Flachsbart, C. Baylis, L. Cohen, R. J. Marks II, "Fast, Momentum-Aided Optimization of Transmitter Amplifier Load Impedance and Input Power for Cognitive Radio using the Power Smith Tube,” 2016 IEEE Radio and Wireless Symposium (RWS), IEEE, 2016.

[40] M. Fellows, S. Rezayat, J. Barlow, J. Barkate, A. Tsatsoulas, C. Baylis, L. Cohen, R. J. Marks II, "The Bias Smith Tube: Simultaneous Optimization of Bias Voltage and Load Impedance in Power-amplifier Design,” 2016 IEEE Radio and Wireless Symposium (RWS), IEEE, 2016.

[41] Hays, L.; Egbert, A.; Kappelmann, C.; Baylis, C.; Marks, R.; Viveiros, E.; “Real-time Transistor Stability Measurements Utilizing Acceleration of the Gain for the Next Generation Radar” USNC-URSI National Radio Science Meeting, January 2018, Boulder, Colorado